

1 **The Seasonal Cycle of pCO₂ and CO₂ fluxes in the Southern Ocean:**
2 **Diagnosing Anomalies in CMIP5 Earth System Models**

3
4 **Precious N. Mongwe^{1,2}, Marcello Vichi^{2,3} & Pedro M.S. Monteiro^{1,2}**

5 ¹**Southern Ocean Carbon-Climate Observatory (SOCCO), CSIR, Cape Town, South Africa**

6 ²**Department of Oceanography, University of Cape Town, Cape Town, South Africa**

7 ³**Marine Research Institute, University of Cape Town, Cape Town, South Africa**

8 pmongwe@csir.co.za

9

10 **Abstract**

11

12 The Southern Ocean forms an important component of the earth system as a major sink of CO₂ and
13 heat. Recent studies based on the Coupled Model Intercomparison Project version 5 (CMIP5) Earth
14 System Models (ESMs) show that CMIP5 models disagree on the phasing of the seasonal cycle of the
15 CO₂ flux (FCO₂) and compare poorly with available observation products for the Southern Ocean.
16 Because the seasonal cycle is the dominant mode of CO₂ variability in the Southern Ocean, its
17 simulation is a rigorous test for models and their long-term projections. Here we examine the
18 competing roles of temperature and dissolved inorganic carbon (DIC) as drivers of the seasonal cycle
19 of pCO₂ in the Southern Ocean to explain the mechanistic basis for the seasonal biases in CMIP5
20 models. We find that despite significant differences in the spatial characteristics of the mean annual
21 fluxes, the intra-model homogeneity in the seasonal cycle of FCO₂ is greater than observational
22 products. FCO₂ biases in CMIP5 models can be grouped into two main categories i.e. group-SST and
23 group-DIC. Group-SST models show an exaggeration of the seasonal rates of change of sea surface
24 temperature (SST) in autumn and spring during the cooling and warming peaks. These higher-than-
25 observed rates of change of SST tip the control of the seasonal cycle of pCO₂ and FCO₂ towards SST and
26 result in a divergence between the observed and modelled seasonal cycles, particularly in the Sub-
27 Antarctic Zone. While almost all analyzed models (9 out of 10) show these SST-driven biases, 3 out of
28 10 (namely NorESM1-ME, HadGEM-ES and MPI-ESM, collectively the group-DIC models) compensate
29 the solubility bias because of their overly exaggerated primary production, such that biologically-
30 driven DIC changes mainly regulate the seasonal cycle of FCO₂.

31

32

33

34

35 **1. Introduction**

36

37 The Southern Ocean (south of 30°S) takes up about a third of the total oceanic CO₂ uptake, slowing
38 down the accumulation of CO₂ in the atmosphere (Fung et al., 2005; Le Quere et al., 2016; Takahashi et
39 al., 2012). The combination of upwelling deep ocean circumpolar waters (which are rich in carbon and
40 nutrients) and the subduction of fresh colder mid-latitude waters makes it a key region in the role of
41 sea-air gas exchange and heat uptake (Barbero et al., 2011; Gruber et al., 2009; Sallée et al., 2013). The
42 Southern Ocean supplies about a third of the total nutrients responsible for biological production
43 north of 30°S (Sarmiento et al., 2004), and accounts for about 75% of total ocean heat uptake
44 (Frölicher et al., 2015). Recent studies suggest that the Southern Ocean CO₂ sink is expected to change
45 as a result of anthropogenic warming, however, the sign and magnitude of the change is still disputed
46 (Leung et al., 2015; Roy et al., 2011; Sarmiento et al., 1998; Segschneider and Bendtsen, 2013). While
47 some studies suggest that the Southern Ocean CO₂ sink is weakening and will continue to do so (e.g. Le
48 Quéré et al., 2007; Son et al., 2010; Thompson et al., 2011), other recent studies infer an increasing CO₂
49 sink (Landschutzer et al., 2015; Takahashi et al., 2012; Zickfeld et al., 2008).

50

51 Although the Southern Ocean plays a crucial role as a CO₂ reservoir and regulator of nutrients and
52 heat, it remains under-sampled, especially during the winter season (JJA) (seasonal cycle in the
53 Southern Hemisphere) (Bakker et al., 2014; Monteiro et al., 2010). Consequently, we largely rely on
54 Earth System Models (ESM), inversions and ocean models for both process understanding and future
55 simulation of CO₂ processes in the Southern Ocean. The Coupled Model Intercomparison Project
56 (CMIP) provides an example of such a globally organized platform (Taylor et al., 2012). Although
57 recent studies based on CMIP5 ESMs, forward and inversions models show that CMIP5 models agree
58 on the CO₂ annual mean sink, they disagree with available observations on the phasing of the seasonal
59 cycle of sea-air CO₂ flux (FCO₂) in the Southern Ocean (e.g. Anav et al., 2013; Lenton et al., 2013).

60

61 The seasonal cycle is a major mode of variability for chlorophyll (Thomalla et al., 2011) and CO₂ in the
62 Southern Ocean (Monteiro et al., 2010; Lenton et al., 2013). The large-scale seasonal states of sea-air
63 CO₂ fluxes (FCO₂) in the Southern Ocean comprise of extremes of strong summer in-gassing with a
64 weaker in-gassing or even out-gassing in winter (Metzl et al., 2006). These extremes are linked by the
65 autumn and spring transitions. In autumn CO₂ in-gassing weakens linked to the increasing
66 entrainment of sub-surface waters, which are rich in dissolved inorganic carbon (DIC), (Lenton et al.,
67 2013; Metzl et al., 2006; Sarmiento and Gruber, 2006). During spring, the increase of primary
68 production consumes DIC at the surface and increases the ocean's capacity to take up atmospheric CO₂
69 (Gruber et al., 2009; Le Quéré and Saltzman, 2013; Pasquer et al., 2015; Gregor et al., 2017). The
70 increase of sea surface temperature (SST) in summer reduces surface CO₂ solubility, which counteracts

71 the biological uptake and reduces the CO₂ flux from the atmosphere (Takahashi et al., 2002; Lenton et
72 al., 2013).

73

74 FCO₂ is also spatially variable in the Southern Ocean at the seasonal scale. North of 50°S is generally
75 the main CO₂ uptake zone (Hauck et al., 2015; Sabine et al., 2004). This region forms a major part of
76 the sub-Antarctic Zone and is characterized by the confluence of upwelled, colder and nutrient-rich
77 deep circumpolar water and mid-latitudes warm water (McNeil et al., 2007; Sallée et al., 2006). It is
78 characterized by enhanced biological uptake during spring and solubility-driven CO₂ uptake due to
79 cool surface waters (Marinov et al., 2006; Metzl, 2009; Takahashi et al., 2012). South of 60°S towards
80 the marginal ice Zone, CO₂ fluxes are largely dominated by out-gassing, driven by the upwelling of
81 circumpolar waters, which are rich in DIC (Matear and Lenton, 2008; McNeil et al., 2007).

82

83 The inability of CMIP5 ESM to simulate a comparable FCO₂ seasonal cycle with available observations
84 estimates in the Southern Ocean has been the subject of recent literature (e.g. Anav et al., 2013;
85 Kessler and Tjiputra, 2016) and the mechanisms associated with these biases are still not well
86 understood. This model-observations disagreement highlights that the current ESMs might not
87 adequately capture the dominant seasonal processes driving the FCO₂ in the Southern Ocean. It also
88 questions the sensitivity of models to adequately simulate the Southern Ocean century-scale CO₂ sink
89 and its sensitivity to climate change feedbacks (Lenton et al., 2013). Efforts to improve simulations of
90 CO₂ properties with respect to observations in the Southern Ocean are ongoing using forced ocean
91 models (e.g. Pasquer et al., 2015; Rodgers et al., 2014; Visinelli et al., 2016; Rosso et al., 2017).
92 However, it remains a challenge for fully coupled simulations. In a previous study, we developed a
93 diagnostic framework to evaluate the seasonal characteristics of the drivers of FCO₂ in ocean
94 biogeochemical models (Mongwe et al., 2016). We here apply this approach to 10 CMIP5 models
95 against observation product estimates in the Southern Ocean. The subsequent analysis is divided as
96 follows; the methods section (section 2) explains our methodological approach, followed by results
97 (section 3), which comprise four subsections. Section 3.1 explores the spatial variability of the annual
98 mean representation of FCO₂ in the 10 CMIP5 models against observation product estimates; section
99 3.2 quantifies the biases in the FCO₂ seasonal cycles in the 10 models. Section 3.3 investigates surface
100 ocean drivers of FCO₂ changes (temperature driven solubility and primary production), and finally,
101 section 3.4 examines the source terms in the DIC surface budget (primary production, entrainment
102 rates and vertical gradients) and their role in surface pCO₂ changes. The discussion (section 4) is an
103 examination of the mechanisms behind the pCO₂ and FCO₂ biases in the models. We conclude with a
104 synthesis of the main findings and their implications.

105

106

107 **2. Methods**

108

109 The Southern Ocean is here defined as the ocean south of the Sub-Tropical Front (STF, defined
110 according to Orsi et al., (1995), 11.3°C isotherm at 100m). It is divided into two main domains, the Sub-
111 Antarctic Zone; between the STF and the Polar Front (PF: 2°C isotherm at 200m) and the Antarctic
112 Zone, south of the PF. Within the Sub-Antarctic Zone and Antarctic Zone, we further partition the
113 domain into the three main basins of the Southern Ocean i.e. Pacific, Atlantic and the Indian zone.

114

115 **2.1 Observations datasets**

116

117 We used the Landschützer et al. (2014) data product (FCO_2 and partial pressure of CO_2 (pCO_2)) as the
118 main suite of observations-based estimates against which to compare the models throughout the
119 analysis. Landschützer et al. (2014) dataset is synthesized from Surface Ocean CO_2 Atlas version 2
120 (SOCAT2) observations and high resolution winds using a Self-Organizing Map (SOM) through a Feed
121 Forward Neural Network (FNN) approach (Landschützer et al., 2013). While Landschützer et al.
122 (2014) dataset is based on more *in situ* observations (SOCAT2, 15 million source measurements)
123 (Bakker et al., 2014) in comparison to Takahashi et al., (2009) (3 million surface measurements), used
124 in Mongwe et al., (2016). We are nevertheless mindful that due to paucity of observations in the
125 Southern Ocean, this data product is still subject to significant uncertainties, as discussed in Ritter et
126 al. (2018). To evaluate the uncertainty between data products we compare the Landschützer et al.
127 (2014) data with Gregor et al. (2017) data product, which is based on two independent empirical
128 models: Support Vector Regression (SVR) and Random Forest Regression (RFR) as well as against
129 Takahashi et al. (2009) for pCO_2 in the Southern Ocean. We compare pCO_2 instead of FCO_2 firstly,
130 because Gregor et al., (2017) only provided fugacity and pCO_2 , and being mindful that the choice of
131 wind product and transfer velocity constant in computing FCO_2 would increase the level of uncertainty
132 (Swart et al., 2014). Secondly, while the focus of the paper is on the examination biases in the air-sea
133 fluxes of CO_2 , the major part of our analysis is based on pCO_2 , which primarily determines the direction
134 and part of the magnitude of the fluxes. We find that the three data products agree on the seasonal
135 phasing of pCO_2 in the Sub-Antarctic Zone, but they show differences in the magnitudes (Fig. S1). In the
136 Antarctic Zone, all three datasets agree in both phasing and amplitude (Fig. S1). At this stage it is not
137 clear whether this agreement is due to all the methods converging even with the sparse data or the
138 reason for agreement is the lack of observations. Nevertheless, more independent *in situ* observations
139 will be helpful to resolve this issue. In this regard float observations from the SOCCOM program
140 (Johnson et al., 2017) and glider observations (Monteiro et al., 2015), for example, are likely to become

141 helpful in resolving these data uncertainties in addition to ongoing ship-based measurements.

142

143 We also used the Takahashi et al. (2009) in situ FCO₂ dataset as a complementary source for
144 comparison of spatial FCO₂ properties in the Southern Ocean. Takahashi et al. (2009) data estimates
145 are comprised of a compilation of about 3 million surface measurements globally, obtained from 1970
146 – 2000 and corrected for reference year 2000. This dataset is used, as provided, on a 4° (latitude) x 5°
147 (longitude) resolution. Using monthly mean sea surface temperature (SST) and salinity from the World
148 Ocean Atlas 2013 (WOA13) dataset (Locarnini et al., 2013), we reconstructed total alkalinity (TAlk)
149 using the Lee et al. (2006) formulation. We also use this dataset as the main observations platform in
150 section 2.3. To calculate the uncertainty of the computed TAlk, we compared the calculated total
151 alkalinity (TAlk_{calc}) based on ship measurements of SST and surface salinity dataset with actual
152 observed TAlk_{obs} of the same measurements for a set of winter (August) data collected in the Southern
153 Ocean. We found that TAlk_{calc} compares well with TAlk_{obs} (R² = 0.79) (Fig. S2, Supplementary). We
154 then used this computed monthly TAlk and pCO₂ from Landschützer et al. (2014) to compute DIC
155 using CO2SYS (Pierrot et al., 2006, http://cdiac.ornl.gov/ftp/co2sys/CO2SYS_calc_XLS_v2.1), using K1,
156 K2 from Mehrbach et al. (1973) refitted by Dickson and Millero (1987). For interior ocean DIC, we
157 used the Global Ocean Data Analysis Project version 2 (GLODAP2) annual means dataset (Lauvset et
158 al., 2016). The Mixed Layer Depth (MLD) data was taken from de Boyer Montégut et al. (2004), on a 1°
159 x 1° grid, the data is provided as monthly means climatology and was used as provided. We also use
160 satellite chlorophyll dataset from Johnson et al. (2013).

161

162 **2.2 CMIP5 Model data**

163

164 We used 10 models from the Coupled Model Intercomparison Project version 5 (CMIP5) Earth System
165 Models (ESM) shown in Table 1. The selection criterion for the models was based on the availability of
166 essential variables for the analysis in the CMIP5 data portal (<http://pcmdi9.llnl.gov>) at the time of
167 writing: i.e. monthly FCO₂, pCO₂, chlorophyll, net primary production (NPP), surface oxygen, surface
168 Dissolved Inorganic Carbon (DIC), MLD, Sea Surface Temperature (SST), vertical temperature fields
169 and annual DIC for the historical scenario. The analysis is primarily based on the climatology over
170 1995 – 2005, which was selected to match a period closest to the available observational data product
171 (Landschützer et al. (2014), 1998 – 2011). However, we do examine the consistency of the seasonality
172 of FCO₂ over periods longer than 10 years by comparing the seasonal cycle of FCO₂ and temporal
173 standard deviation of 30 years (1975 – 2005) vs 10 years (1995 – 2005) for HadGEM2-ES and
174 CanESM2. We find that the seasonal cycle of FCO₂ remains consistent (R = 0.99) in both HadGEM2-ES

175 and CanESM2 over 30 years (Fig. S3). All CMIP5 model outputs were regridded into a common 1°x1°
 176 regular grid throughout the analysis, except for annual CO₂ mean fluxes, which were computed on the
 177 original grid for each model.

178

179 **Table 1:** A description of the 10 CMIP5 ESMs that were used in this analysis. It shows the ocean
 180 resolution, atmospheric resolution, and available nutrients for the biogeochemical component, sea-ice
 181 model, vertical levels and the marine biogeochemical component for each ESM.

182

| Full name and Source | Model Name | Ocean Resolution | Atmospheric Resolution | Nutrients | Sea ice model | Vertical Coordinate & Levels | Ocean Biology | Reference |
|---|--------------|------------------------|------------------------|-----------------------------------|---------------|------------------------------|---------------|-----------------------|
| Canadian Centre for Climate Modelling and Analysis, Canada | CanESM2 | CanOM4 0.9°x1.4° | 2.8125° x 2.8125° | N (accounts for Fe limitation) | CanSIM1 | z 40 levels | NPZD | Zahariev et al., 2008 |
| Centro Euro-Mediterraneo Sui Cambiamenti Climatici, Italy | CMCC-CESM | OPA8.2 0.5-2°x2° | 3.8° x 3.7° | P, N, Fe, Si | CICE4 | z 21 levels | PELAGOS | Vichi et al., 2007 |
| Centre National de Recherches Météorologiques-Centre Européen de Recherche et de Formation Avancée en Calcul Scientifique, France | CNRM-CM5 | NEMOv3.3 1° | 1.4° | P, N, Fe, Si | GELATO5 | z 42 levels | PISCES | Séférián et al., 2013 |
| Institut Pierre-Simon Laplace, France | IPSL-CM5A-MR | NEMO2.3 0.5-2° x 2° | 2.58° x 1.25° | P, N, Fe, Si | LIM2 | z 31 levels | PISCES | Séférián et al., 2013 |
| Max Planck Institute for Meteorology, Germany | MPI-ESM-MR | MPIOM 1.41°x0.89° | 1.875° x 1.875° | P, N, Fe, Si | MPIOM | z 40 levels | HAMOC5.2 | Ilyina et al., 2013 |

| | | | | | | | | |
|--|------------|----------------------|--------------|-----------------------------|----------|------------------|-------------|-----------------------------|
| Community Earth System Model, USA | CESM1-BGC | 0.3° x 1° | 0.9° x 1.25° | (P), N, Fe, Si | | z 60 levels | BEC | Moore et al., 2004 |
| Norwegian Earth System Model, Norway | NorESM1-ME | MICOM 0.5° x 0.9° | 2.5° x 1.9° | P, N, Fe, Si | CICE4.1 | ρ 53 levels | HAMOCC | Tjiputra et al., 2013 |
| Geophysical Fluid Dynamics Laboratory Earth System Model, USA | GFDL-ESM2M | 0.3° x 1° | 2.5° x 2.0° | N, P, SiO ₄ , Fe | SISp2 | z 50 levels | TOPAZ2 | Dunne et al., 2013 |
| Meteorological Research Institute-Earth System Model Version 1, Japan | MRI-ESM | 0.5° x 1° | | P,N | MRI.COM3 | σ-z 51 levels | NPZD | Adachi et al., 2013 |
| Hadley Global Environment Model 2 - Earth System, UK | HadGEM-ES | 0.3° x 1° | 2.5° x 2.0° | N,Fe,S | | 40 levels | Diat-HadOCC | Palmer and Totterdell, 2001 |

183

184

185 **2.3 Sea-Air CO₂ Flux Drivers: The Seasonal Cycle Diagnostic Framework**

186

187 The seasonal cycle of the ocean-atmosphere pCO₂ gradient ($\Delta p\text{CO}_2$) is the main driver of the variability
188 of FCO₂ over comparable periods (Sarmiento and Gruber, 2006; Wanninkhof et al., 2009; Mongwe et
189 al., 2016). Wind speed plays a dual role as a driver of FCO₂: it drives the seasonal evolution of
190 buoyancy-mixing dynamics, which influences the biogeochemistry and upper water column physics
191 (but these processes are incorporated into the variability of the DIC), as well as the rate of gas
192 exchange across the air-sea interface (Wanninkhof et al., 2013). However, because winds in the
193 Southern Ocean do not have large seasonal variation (Young, 1999), for this analysis, we neglect the
194 role of wind as a secondary driver of the seasonal cycle of FCO₂. Consequently, the seasonal cycle of
195 FCO₂ is directly linked to surface pCO₂ variability, influenced by changes in temperature, salinity, TALK
196 and DIC and macronutrients (Sarmiento and Gruber, 2006; Wanninkhof et al., 2009). In this analysis
197 we use this assumption as a basis to explore how the seasonal variability of temperature and DIC
198 regulate the seasonal cycle of pCO₂ in CMIP5 models relative to observational product estimates.

199

200 The seasonal cycle diagnostic framework was developed as a way of scaling the relative contributions

201 from the rates of change of SST- and the total DIC-driven changes to the seasonal cycle of pCO₂ on to a
 202 common DIC scale (Mongwe et al., 2016). We use the framework to explore how understanding
 203 differences emerging from the temperature- and DIC-driven CO₂ variability could be helpful as a
 204 diagnostic of the apparent observations –model seasonal cycle biases in the Southern Ocean.

205

206 The total rate of change of DIC in the surface layer consists of the contribution of air-sea exchanges,
 207 biological, vertical and horizontal transport-driven changes (Eq. 1).

208

$$209 \left(\frac{\partial DIC}{\partial t} \right)_{Tot} = \left(\frac{\partial DIC}{\partial t} \right)_{air-sea} + \left(\frac{\partial DIC}{\partial t} \right)_{Bio} + \left(\frac{\partial DIC}{\partial t} \right)_{Vert} + \left(\frac{\partial DIC}{\partial t} \right)_{Hor} \quad (1)$$

210 Because we used zonal means from medium resolution models, we assume that the horizontal terms
 211 are negligible, though mindful that there could be a seasonal cycle in the divergence of the horizontal
 212 transport due to a latitudinal gradient in DIC perturbed by Ekman flow in some regions of the Sub-
 213 Antarctic Zone (Rosso et al., 2017). This leaves air-sea exchange, vertical fluxes (advection and
 214 diffusion) and biological processes as the dominant drivers of DIC.

215 Since temperature does not affect DIC changes directly, but only pCO₂ through solubility, it was
 216 necessary to scale the influence of temperature into equivalent DIC units in order to compare the
 217 influence of temperature vs DIC control of surface pCO₂ variability. Thus in order to constrain the
 218 contribution of temperature on the seasonal variability of pCO₂ and FCO₂ we derived a new synthetic
 219 temperature-linked term “DIC equivalent” (DIC_T) defined as: *the magnitude of DIC change that would*
 220 *correspond to a change in pCO₂ driven by a particular temperature change.* In this way the ΔpCO₂
 221 driven solely by modelled or observed temperature change, is converted into equivalent DIC units,
 222 which allows its contribution to be scaled against the observed or modelled total surface DIC change
 223 (Eq.1). Shifts between temperature and DIC control of pCO₂ are in effect tipping points because they
 224 reflect major shifts in the mechanisms that drive pCO₂ variability. We use this as the basis to
 225 investigate the possible mechanisms behind model biases in the seasonal cycle of pCO₂.

226 This calculation of DIC_T is done in two steps: firstly, the temperature impact on pCO₂ is calculated
 227 using the Takahashi et al. (1993) empirical expression that linearizes the temperature dependence of
 228 the equilibrium constants.

$$229 \left(\frac{\partial pCO_2}{\partial t} \right)_{SST} = 0.0423 \times pCO_2 \times \left(\frac{\partial pCO_2}{\partial SST} \right) \quad (2)$$

230 Though this relationship between dSST and dpCO₂ is based on a linear assumption (Takahashi et al.,
 231 1993), this formulation has been shown to hold and has been widely used in literature (e.g. Bakker et
 232 al., 2014; Feely et al., 2004; Marinov and Gnanadesikan, 2011; Takahashi et al., 2002; Wanninkhof et

233 al., 2009; Landschützer et al., 2018). We show in the supplementary material that the extension of this
 234 expression into polar temperature ranges (SST < 2°C) only introduces a minor additional uncertainty
 235 of 4 -5% (SM Fig. S4).

236 Secondly, the temperature-driven change in pCO₂ is converted to an equivalent DIC_T using the Revelle
 237 factor.

$$238 \left(\frac{\partial DIC_T}{\partial t} \right)_{SST} = \frac{DIC}{\gamma_{DIC} \times pCO_2} \left(\frac{\partial pCO_2}{\partial t} \right)_{SST} \quad (3)$$

239 Here we also used a fixed value for the Revelle Factor ($\gamma_{DIC}=14$), typical of polar waters in the Southern
 240 Ocean in order to assess the error linked to this assumption. We recomputed the Revelle factor in the
 241 Sub-Antarctic and Antarctic Zones using annual mean climatologies of TALK, salinity, sea surface
 242 temperature and nutrients. Firstly, we examined DIC changes for the nominal range of pCO₂ change
 243 (340 – 399 μ atm:1 μ atm intervals) and then used this dataset to derive the Revelle factor. The range of
 244 calculated Revelle factors in the Southern Ocean was between $\gamma_{DIC} \sim 12 - 15.5$ with an average of $\gamma_{DIC} =$
 245 13.9 ± 1.3 . This justifies our use of $\gamma_{DIC} = 14$ for the conversion of the solubility-driven pCO₂ change to
 246 an equivalent DIC (DICT) throughout the analysis. We have provided the uncertainty that this
 247 conversion makes into the temperature constraint DIC_T, by using the upper and lower limits of the
 248 Revelle factor ($\gamma_{DIC} = 12 - 15.5$) in the model framework. In the Supplementary Material (Fig. S5) we
 249 show examples for observations in the Sub-Antarctic and Antarctic Zones, which indicate that the
 250 extremes of the Revelle factor values ($\gamma_{DIC} = 12 - 15.5$) do not alter the phasing or magnitude of the
 251 relative controls of temperature or DIC on the seasonal cycle of pCO₂.

252 The rate of change of DIC was discretized on a monthly mean as follows:

$$254 \left(\frac{\partial DIC_T}{\partial t} \right)_{SST} \approx \left(\frac{\Delta DIC}{\Delta t} \right)_{n,l} = \frac{DIC_{n+1,l} - DIC_{n,l}}{1 \text{ month}} \quad (4)$$

255

256 Where n is time in month, l is vertical level (in this case the surface, l=1). We here take the forward
 257 derivative such that November rate is the difference between 15 November and 15 December, thus
 258 being centered at the interval between the months.

259 Finally, to characterize periods of temperature or DIC dominance as main drivers of the instantaneous
 260 (monthly) pCO₂ change we subtract Eq. 1 from Eq. 4, which yields a residual indicator M_{T-DIC} Eq. 5. M_{T-}

261 DIC is then used as indicator of the dominant driver of instantaneous pCO₂ changes in this scale monthly
 262 time scale.

263

$$264 \quad M_{T-DIC} = \left| \left(\frac{\partial DIC_T}{\partial t} \right)_{SST} \right| - \left| \left(\frac{\partial DIC}{\partial t} \right)_{Tot} \right| \quad (5)$$

265

266 M_{T-DIC} > 0 indicates that the pCO₂ variability is dominated by the temperature-driven solubility and
 267 when M_{T-DIC} < 0, it indicates that pCO₂ changes are mainly modulated by DIC processes (i.e. Biological
 268 CO₂ changes and vertical scale physical DIC mechanisms). We also examine the following DIC
 269 processes; i.) Biological DIC changes using chlorophyll, NPP, export carbon, surface oxygen, and ii.).
 270 Physical DIC mechanisms using estimated entrainment rates at the base of the mixed layer. Details of
 271 this calculation are in section 2.4.

272 In the Southern Ocean, salinity and TAlk are considered lower-order drivers of the seasonal cycle of
 273 pCO₂ (Takahashi et al., 1993). In the supplementary material (Fig. S6), we show that salinity and TAlk
 274 do not play a major role as drivers of the local seasonal cycle of pCO₂. We do so by computing the
 275 equivalent rate of change of DIC resulting from seasonal variability of salinity and TAlk as done for
 276 temperature (Eq. 2), i.e. still assuming empirical linear relationships from Takahashi et al. (1993):

$$277 \quad \left(\frac{\ln(pCO_2)}{\ln(TAlk)} \approx -9.4 \right) \text{ and } \left(\frac{\ln(pCO_2)}{\ln(Sal)} = 0.94 \right). \text{ By applying these relationships to the model data, we}$$

278 confirmed that indeed salinity and TAlk are secondary drivers of pCO₂ changes i.e. $\left[\left(\frac{\partial DIC}{\partial t} \right)_{Tot} \right]_{average} \approx$

$$279 \quad 5 \mu\text{mol kg}^{-1} \text{ month}^{-1}, \text{ while } \left[\left(\frac{\partial DIC}{\partial t} \right)_{Tot} \right]_{average} \approx 0.6 \mu\text{mol kg}^{-1} \text{ month}^{-1} \text{ and } \left[\left(\frac{\partial DIC}{\partial t} \right)_{TAlk} \right]_{maximum} \approx 0.4$$

280 $\mu\text{mol kg}^{-1} \text{ month}^{-1}$.

281

282 **2.4 Entrainment mixing**

283

284 CO₂ uptake by the Southern Ocean has been shown to weaken during winter linked to the entrainment
 285 of sub-surface DIC as the MLD deepens (e.g. Lenton et al., 2013; Metzl et al., 2006; Takahashi et al.,
 286 2009). Here we estimate this rate of entrainment (RE) using Eq. 6, which estimates the advection of
 287 preformed DIC at the base of the mixed layer:

288

$$289 \quad RE = U_e \left(\frac{\partial DIC}{\partial z} \right)_{MLD} \quad (6)$$

$$290 \quad RE_n = \left(\frac{\Delta MLD_n}{\Delta t} \right) \left(\frac{\Delta DIC}{\Delta z} \right)_{n,MLD} \quad (7)$$

$$291 \quad \left(\frac{\Delta DIC}{\Delta z} \right)_{n,MLD} = \frac{DIC_{n,MLD_{n+1}} - DIC_{n,MLD_n}}{\Delta z} \quad (8)$$

292

293 In which U_e is an equivalent entrainment velocity based on the rate of change of the MLD and n is the
294 time in months. This approximation of vertical entrainment is necessary as it is not possible to
295 compute this term from the CMIP5 data because the vertical DIC distribution is only available as an
296 annual means. We use the entrainment rates to estimate the influence of subsurface/bottom DIC
297 changes on surface DIC changes and subsequently $p\text{CO}_2$ and FCO_2 . Because we are mainly interested in
298 the period autumn- winter, where the MLD ≥ 60 m in the Sub-Antarctic Zone and ≥ 40 m in the
299 Antarctic Zone at this depth seasonal variations in DIC are anticipated to be minimal – these estimates
300 can be used. The monthly and annual mean DIC from a NEMO PISCES $0.5 \times 0.5^\circ$ model output were
301 used to estimate the uncertainty by comparing RE computed from both (Dufour et al., 2013). We found
302 the annual and monthly estimates to be indeed comparable with minimal differences (not shown). It is
303 noted as a caveat that this rate of entrainment is only a coarse estimate because we were using annual
304 means, and is intended only for the autumn-winter period when MLDs are deepened.

305

306 **3. Results**

307

308 **3.1 Annual climatological sea-air CO_2 fluxes**

309

310 The annual mean climatological distribution of FCO_2 in the Southern Ocean obtained from
311 observational products is spatially variable, but mainly characterized by two key features: (i) CO_2 in-
312 gassing north of 50°S - 55°S (Polar Frontal Zone, PFZ) within and north of the Sub-Antarctic Zone, and
313 (ii), CO_2 out-gassing between the PF ($\sim 58^\circ\text{S}$) and the Marginal Ice Zone (MIZ, $\sim 60^\circ - 68^\circ\text{S}$) (Fig. 1a-b).
314 Most CMIP5 models broadly capture these features, however, they also show significant differences in
315 space and magnitude between the basins of the Southern Ocean (Fig. 1). With the exception of CMCC-
316 CESM, which shows a northerly-extended CO_2 out-gassing band between about 40°S and 50°S , CMIP5
317 models generally show the CO_2 out-gassing zone between 50°S - 70°S in agreement with observational
318 estimates (Fig. 1).

319

320 The analyzed 10 CMIP5 models show a large spatial dispersion in the spatial representation of the
321 magnitudes of FCO_2 with respect to observations (Fig. 1, Table 2). They generally overestimate the
322 upwelling-driven CO_2 out-gassing (55°S - 70°S) in some basins relative to observations. IPSL-CM5A,
323 CanESM2, MPI-ESM, GFDL-ESM2M and MRI-ESM, for example, show CO_2 out-gassing fluxes reaching
324 up to $25 \text{ g m}^{-2} \text{ yr}^{-1}$, while observations only show a maximum of $8 \text{ g m}^{-2} \text{ yr}^{-1}$ (Fig. 1). Between 40°S -
325 56°S (Sub-Antarctic Zone), observations and CMIP5 models largely agree, showing a CO_2 in-gassing
326 feature, which is mainly attributable to biological processes (McNeil et al., 2007; Takahashi et al.,
327 2012). South of 65°S , in the MIZ, models generally show an excessive CO_2 in-gassing with respect to

328 observations (with the exception of CanESM2, IPSL-CM5A-MR and CNRM-CM5). Note that as much as
329 this bias south of the MIZ might be a true divergence of CMIP5 models from the observed ocean, it is
330 also possibly due to the lack of observations in this region, especially during the winter season (Bakker
331 et al., 2014; Monteiro, 2010).

332
333 Table 2 shows the Pattern Correlation Coefficient (PCC) and the Root Mean Square Error (RMSE),
334 which are here used to quantify the model spatial and magnitude performances against Landschützer
335 et al. (2014) data product. Out of the 10 models, six show a moderate spatial correlation with
336 Landschützer et al. (2014) (PCC = 0.40 – 0.60), i.e. CNRM-CM5, GFDL-ESM2M, HadGEM2-ES, IPSL-
337 CM5A-MR, CESM1-BGC, NorESME-ME and CanESM2. While MPI-ESM-MR (PCC = 0.37), MRI-ESM (PCC
338 = 0.36) and CMCC-CESM (PCC = -0.09) show a weak to null spatial correlation with observations, the
339 latter is mainly due to the overestimated out-gassing region. Spatially, GFDL-ESM2M and NorESM1-ME
340 are the most comparable to Landschützer et al. (2014), (RMSE < 9), while CCMC-CESM, CanESM2, MRI-
341 ESM and CNRM-CM5 shows the most differences (RMSE > 15). The rest of the models show a modest
342 comparison (RMSE 9 – 11).

343
344 NorESM1-ME and CESM1-BGC are the only two of the 10 models showing a consistent spatial (RMSE
345 < 9) and magnitude (PCC \approx 0.50) performance. From Table 2, it is evident that an appropriate
346 representation of the spatial properties of FCO₂ with respect to observations does not always
347 correspond to comparable magnitudes. CanESM2 for example, shows a good spatial comparison (PCC
348 = 0.54), yet a poor estimation of the magnitudes (RMSE = 19.5). In this case this is caused by an
349 overestimation of CO₂ uptake north of 55°S (\approx - 28 g m⁻² yr⁻¹) and CO₂ out-gassing (> 25 g m⁻² yr⁻¹) in
350 the Antarctic zone, resulting in a net total Southern Ocean annual weak sink (-0.05 Pg C m⁻² yr⁻¹).

351

352 **3.2 Sea-Air CO₂ Flux Seasonal Cycle Variability and Biases**

353

354 The seasonal cycle of FCO₂ is shown in Fig. 2. The seasonality of FCO₂ in the 10 CMIP5 models shows a
355 large dispersion in both phasing and amplitude, but mostly disagrees with observations in the phase of
356 the seasonal cycle as well as disagreeing with each other. More quantitatively, CMIP5 models show
357 weak to negative correlations with the Landschützer et al. (2014) data product in the Sub-Antarctic
358 Zone and have slightly higher correlations in the Antarctic Zone (see supplementary Fig. S7). This
359 discrepancy is consistent with the findings of Anav et al. (2013), who however used fixed latitude
360 criteria. Based on the phasing, the seasonality of FCO₂ in CMIP5 models can be a priori divided in two
361 main groups: group-DIC models, comprising of MPI-ESM, HadGEM-ES and NorESM1-ME, and group-
362 SST models, the remainder i.e. GFDL-ESM2M, CMCC-CESM, CNRM-CERFACS, IPSL-CM5A-MR, CESM1-
363 BGC, MRI-ESM and CanESM2. The naming convention is suggestive of the mechanism driving the

364 seasonal cycle, as will be clarified further on. A similar grouping was also identified by Kessler and
365 Tjiputra (2016) using a different criterion. Fig. 3 shows the seasonal cycle of FCO_2 of an equally-
366 weighted ensemble of the two groups compared to observations; the shaded area shows the decadal
367 standard deviation for the models and the Landschützer et al. (2014) data product for 1998-2014
368 standard deviation in the various regions.

369
370 In the Sub-Antarctic Zone, the observational products show a weakening of CO_2 uptake during winter
371 (less negative values in June-August) with values close to the zero at the onset of spring (September)
372 in all three basins. Similarly, during the spring season, all three basins are seen to maintain a steady
373 increase of CO_2 uptake until mid-summer (December), while they differ during autumn (March-May).
374 The Pacific basin shows an increase in CO_2 uptake during autumn that is not observed in the other
375 basins (only marginally in the Indian zone). In the Antarctic zone, the observed FCO_2 seasonal cycle is
376 mostly similar in all three basins (Fig. 3d-f). While this seasonal cycle consistency may suggest a
377 spatial uniformity of the mechanisms of FCO_2 at the Antarctic, we are also mindful that this may be due
378 to a result of the paucity of observations in this area. In the Antarctic Zone, all three basins show a
379 weakening of uptake or increasing of out-gassing from the onset of autumn (March) until mid-winter
380 (June-July). The winter CO_2 out-gassing is followed by a strengthening of the CO_2 uptake throughout
381 spring to summer, when it reaches a CO_2 in-gassing peak.

382
383 The differences in the seasonal cycle of FCO_2 across the three basins of the Sub-Antarctic Zone found in
384 the observational product (Fig. 2) are likely a consequence of spatial differences seen in Fig. 1. To
385 verify this, we calculated the correlation between the seasonal cycles from the Landschützer et al.
386 (2014) observational product in the three basins (Fig. 4). The FCO_2 seasonal cycle in the Sub-Antarctic
387 Atlantic and Indian basins are similar ($R = 0.8$), while the other basins are quite different to one
388 another ($R = -0.1$ for Pacific – Atlantic and $R \sim 0.4$ for Pacific – Indian). Contrary to the observational
389 product, CMIP5 models show the same seasonal cycle phasing across all three basins in the Sub-
390 Antarctic Zone (basin – basin correlation coefficients are always larger than 0.50 in Fig. 4 despite the
391 spatial differences in Fig. 2, with the exception of three models (i.e. CMCC-CESM, CESM-BGC1 and
392 GFDL-ESM2M)). Thus, contrary to Landschützer et al. (2014), CMIP5 models shows a zonal
393 homogeneity in the seasonal cycle of FCO_2 , which may suggest that the drivers of CO_2 are less regional.
394 In the Antarctic Zone, CMIP5 models agree with observations in the spatial uniformity of the seasonal
395 cycle of FCO_2 across the three basins.

396
397 Group-DIC models are characterized by an exaggerated CO_2 uptake during spring-summer (Fig. 3) with
398 respect to observation estimates and CO_2 out-gassing during winter. These models generally agree
399 with observations in the phasing of CO_2 uptake during spring, but overestimate the magnitudes. It is

400 worth noting that the seasonal characteristics of group-DIC models are mostly in agreement with the
401 observations in the Atlantic and Indian basin in Sub-Antarctic Zone ($R > 0.5$ in Fig. 4). The large
402 standard deviation ($\sim 0.01 \text{ g C m}^{-2} \text{ day}^{-1}$) during the winter and spring-summer seasons in the Atlantic
403 basin shows that though group-DIC models agree in the phase, magnitudes vary considerably (Fig. 3b).
404 For example MPI-ESM reaches up to $0.06 \text{ g C m}^{-2} \text{ day}^{-1}$ out-gassing during winter, while HadESM2-ES
405 and NorESM2 peak only at $\sim 0.03 \text{ g C m}^{-2} \text{ day}^{-1}$. Group-SST models on the other hand are characterized
406 by a CO_2 out-gassing peak in summer (Dec-Feb) and a CO_2 in-gassing peak at the end of autumn (May),
407 and their phase is opposite to the observational estimates in the Atlantic and Indian basins (Fig. 3b,c).
408 Group-SST models only show a strengthening of CO_2 uptake during spring in the Indian basin.
409 Interestingly, group-SST models compare relatively well with the observed FCO_2 seasonal cycle in the
410 Pacific basin, whereas group-DIC models disagree the most with the observed estimates (Fig. 3a). This
411 phasing difference within models and against observed estimates probably suggests that the
412 disagreement of CMIP5 models FCO_2 with observations is not a matter of a relative error/constant
413 magnitude offset, but most likely points to differences in the seasonal drivers of FCO_2 .

414

415 In the Antarctic Zone (Fig. 3d-f), both group-DIC and group-SST models perform better than in the
416 Sub-Antarctic, in respect of phasing and amplitude in as shown by the correlation analysis in Fig. S7.
417 Models reflect comparable pCO_2 seasonality in the different basins of the AZ to the observational
418 products (Fig. 4, with the exception of MRI-ESM and CanESM2 where $R < 0$ for all three basins). Here
419 FCO_2 magnitudes oscillate around zero with the largest disagreements occurring during mid-summer,
420 where observation estimates show a weak CO_2 sink ($\approx -0.03 \text{ gC m}^{-2} \text{ day}^{-1}$), and group-SST show a zero
421 net CO_2 flux and a strong uptake in group DIC (e.g. $\approx -0.12 \text{ gC m}^{-2} \text{ day}^{-1}$ in the Pacific basin). The large
422 standard deviation ($\approx 0.01 \text{ gC m}^{-2} \text{ day}^{-1}$) here indicates considerable differences among models (Fig.
423 3d-f).

424

425 **3.3 Seasonal Scale Drivers of Sea-Air CO_2 Flux**

426

427 We now examine how changes in temperature and DIC regulate FCO_2 variability at the seasonal scale
428 following the method described in Sec. 2.3. Fig. 5 shows the monthly rates of change of SST (dSST/dt)
429 for the 10 models compared with WOA13 SST. CMIP5 generally shows agreement in the timing of the
430 switch from surface cooling ($\text{dSST}/\text{dt} < 0$) to warming ($\text{dSST}/\text{dt} > 0$) and vice versa; i.e. March
431 (summer to autumn), and September (winter to spring) respectively. In both the Sub-Antarctic and
432 Antarctic Zone CMIP5 models agree with observations in this timing (Fig. 5). However, while they
433 agree in phasing, the amplitude of these warming and cooling rates are overestimated with respect to
434 the WOA13 dataset with the exception of NorESM1-ME. Subsequently these differences in the
435 magnitude of dSST/dt have important implications for the solubility of CO_2 in seawater; larger

436 magnitudes of $|dSST/dt|$ are likely to enhance the response of the pCO_2 to temperature through CO_2
437 solubility changes. For example, because the observations in the Indian basin show a warming rate of
438 about $0.5^\circ C \text{ month}^{-1}$ lower compared to the other two basins, we expect a relatively weaker role of
439 surface temperature in this basin.

440
441 As described in sec. 2.3, the computed $dSSt/dt$ magnitudes were used to estimate the equivalent rate
442 of change of DIC driven by CO_2 solubility using Eq. 2. The seasonal cycle of $|(dDIC_T/dt)_{SST}|$ vs
443 $|(dDIC/dt)_{Tot}|$, for the 10 models and observations is presented in the supplementary material (Fig.
444 S8) where we show the seasonal mean of M_{T-DIC} from (Eq. 3). As articulated in sec. 2.3, M_{T-DIC} (Fig. 6) is
445 the difference between the total surface DIC rate of change of DIC (Eq. 1) and the estimated equivalent
446 temperature-driven solubility DIC changes Eq. 3, such that when $|(dDIC_T/dt)_{SST}| > |(dDIC/dt)_{Tot}|$,
447 temperature is the dominant driver of the instantaneous pCO_2 changes, and conversely when $|$
448 $(dDIC_T/dt)_{SST}| < |(dDIC/dt)_{Tot}|$, DIC processes are the dominant mode in the instantaneous pCO_2
449 variability. The models showing the former feature are SST-driven and belong to group-SST, while the
450 models showing the latter are DIC-driven and belong to group-SST.

451
452 According to the M_{T-DIC} magnitudes in Fig. 6, the seasonal cycle of pCO_2 in the observational estimates
453 is predominantly DIC-driven most of the year in both the Sub-Antarctic and Antarctic Zone. Note that,
454 however, during periods of high $|dSST/dt|$, i.e. autumn and spring, observations show a moderate to
455 weak DIC control ($M_{T-DIC} \approx 0$). The Antarctic Zone is mostly characterized by a stronger DIC control
456 (mean Annual $M_{T-DIC} > 3$) except for during the spring season (Fig. 6). Consistent with the similarity
457 analysis presented in Fig. 4, the Antarctic Zone shows coherence in the sign of the temperature –DIC
458 indicator ($M_{T-DIC} > 0$) within the three basins.

459

460

461 **3.4 Source terms in the DIC surface budget**

462

463 To further constrain the surface DIC budget in Eq. 1, we examine the role of the biological source term
464 using chlorophyll and Net Primary Production (NPP) as proxies. Fig. 8 shows the seasonal cycle of
465 chlorophyll, NPP and the rate of surface DIC changes ($dDIC/dt$). The observed seasonal cycle of
466 chlorophyll (Johnson et al., 2013) shows a similar seasonal cycle within the three basins during the
467 spring-summer seasons (autumn-winter data are removed due to the satellite limitation) in both the
468 Sub-Antarctic and Antarctic Zone. Magnitudes are however different in the Sub-Antarctic Zone; the
469 Atlantic basin shows larger chlorophyll magnitudes (Chlorophyll reach up to 1.0 mg m^{-3}) compared to
470 the Pacific and Indian basins ($Chl < 1 \text{ mg m}^{-3}$).

471

472 CMIP5 models here show a clear partition between group-DIC and group-SST models. While they
473 mostly maintain the same phase, group-DIC shows larger amplitudes of chlorophyll relative to group-
474 SST and observed estimates in the Sub-Antarctic Zone. This difference is even clearer in NPP
475 magnitudes, where group-DIC models show a maximum of $NPP > 1 \text{ mmol m}^{-2} \text{ s}^{-1}$ in summer, while
476 group-SST magnitudes shows about half of it. Except for CESM1-BGC and CMCC-CESM (and NorESM1-
477 ME for NPP), each CMIP5 model generally maintains a similar chlorophyll seasonal cycle (phase and
478 magnitude) in all three basins of the Southern Ocean. This is contrary to the observations, which show
479 differences in the magnitude. Consistent with the observational product, CESM1-BGC simulates larger
480 amplitude in the Atlantic basin. While CMCC-CESM also has this feature, it also shows an
481 overestimated chlorophyll peak in the Indian basin. In the Antarctic Zone both observations and
482 CMIP5 models generally agree in both phase and magnitude (except for CanESM2) of the seasonal
483 cycle of chlorophyll in all three basins.

484
485 We now examine the influence of the vertical DIC rate in Eq. 1, using estimated entrainment rates (RE,
486 Eq. 5) based on MLD and vertical DIC gradients (see sec. 2.3). Fig. 7 shows the seasonal changes of
487 MLD compared with the rate from the observational product. CMIP5 models largely agree on the
488 timing of the onset of MLD deepening (February in the Pacific basin, and March for the Atlantic and
489 Indian basin) and shoaling (September) in the Sub-Antarctic Zone (with the exception of NorESM1-ME
490 and IPSL-CM5A in the Pacific basin). The Indian basin generally shows deeper winter MLD in both
491 observations and CMIP5 models in the Sub-Antarctic Zone. Note that while CMIP5 models generally
492 show the observed deeper MLDs in the Indian basin, they show a large variation; for example, the
493 winter maximum depth ranges from 100 m (CMCC-CESM, Pacific basin) to 350 m (CanESM2, Indian
494 basin) in the Sub-Antarctic Zone. In the Antarctic Zone CMIP5 models are largely in agreement on the
495 timing of the onset of MLD deepening (February), but also variable in their winter maximum depth. It
496 is worth noting that the observed MLD seasonal cycle might be biased due to limited in situ
497 observations particularly in the Antarctic Zone (de Boyer Montégut et al., 2004).

498
499 The estimated RE values in Fig. 10 show that almost all CMIP5 (with the exception of NorESM1-ME)
500 entrain subsurface DIC into the mixed layer during autumn–winter in agreement with the
501 observational estimates. In the Sub-Antarctic Zone, the estimates using the observational products
502 show the strongest entrainment in the Atlantic basin in May (RE reaches up to $10 \text{ } \mu\text{mol kg}^{-1} \text{ month}^{-1}$),
503 while it is lower in the other basins. In the Antarctic Zone, observed RE conversely shows stronger
504 entrainment rates in the Pacific and Indian basin ($RE > 15 \text{ } \mu\text{mol kg}^{-1} \text{ month}^{-1}$) in comparison to the
505 Atlantic basin ($RE = 11 \text{ } \mu\text{mol kg}^{-1} \text{ month}^{-1}$). CMIP5 models entrainment rates are variable but not
506 showing any particular deficiency when compared with the observational estimates. Also, the group-
507 DIC and group-SST models show no clear distinction, the major striking features being the relatively

508 stronger entrainment in MPI-ESM and CanESM2 across the three basins in the Sub-Antarctic Zone in
509 mid to late winter ($RE = 15 \mu\text{mol kg}^{-1} \text{ month}^{-1}$), and the large winter entrainment in IPSL-CM5A-MR in
510 the Antarctic Pacific basin. The supply of DIC to the surface due to vertical entrainment is therefore
511 generally comparable between model simulations and the available estimate.

512
513 However, our RE estimates are estimated at the base of the mixed layer, which is not necessarily a
514 complete measure of the vertical flux of DIC at the surface. We therefore investigate the annual mean
515 vertical DIC gradients in Fig. 10 as an indicator of where the surface uptake processes occur. The
516 simulated CMIP5 profiles are similar to GLODAP2, but some differences arise. In the Sub-Antarctic
517 Zone, GLODAP2 shows a shallower surface maximum in the Atlantic basin consistent with higher
518 biomass in this basin ($(dDIC/dz)_{\text{max}} = 0.55 \mu\text{mol kg}^{-1} \text{ m}^{-1}$, at 50 m) compared to the Pacific
519 ($(dDIC/dz)_{\text{max}} = 0.60 \mu\text{mol kg}^{-1} \text{ m}^{-1}$, at 80 m) and Indian basin ($(dDIC/dz)_{\text{max}} = 0.40 \mu\text{mol kg}^{-1} \text{ m}^{-1}$, at
520 80 m). CMIP5 models generally do not show this feature in the Sub-Antarctic Zone, except for CESM1-
521 BGC1 ($(dDIC/dz)_{\text{max}} = 0.50 \mu\text{mol kg}^{-1} \text{ m}^{-1}$, at 50 m). Instead, they show the surface maxima at the same
522 depth in all three basins. In the Antarctic Zone both CMIP5 models and observations show larger
523 $(dDIC/dz)_{\text{max}}$ magnitudes and nearer surface maxima (with the exception of CanESM2 and CESM1-
524 BGC). This difference in the position and magnitude of the DIC maxima between the Sub-Antarctic and
525 Antarctic Zone has important implications for surface DIC changes and subsequently $p\text{CO}_2$ seasonal
526 variability. Because of the nearer surface DIC maxima in the Antarctic Zone, surface DIC changes are
527 mostly influenced by these strong near-surface vertical gradients than MLD changes. This implies that
528 even if the entrainment rates at the base of the MLD are comparable between the Sub-Antarctic and
529 the Antarctic, the surface supply of DIC may be larger in the Antarctic Zone.

530

531

532 **4. Discussion**

533

534 Recent studies have highlighted that important differences exist between the seasonal cycle of $p\text{CO}_2$ in
535 models and observations in the Southern Ocean (Lenton et al., 2013; Anav et al., 2015; Mongwe, 2016).
536 Paradoxically, although the models may be in relative agreement for the mean annual flux, they
537 diverge in the phasing and magnitude of the seasonal cycle (Lenton et al., 2013; Anav et al., 2015;
538 Mongwe, 2016). These differences in the seasonal cycle raise questions about the climate sensitivity of
539 the carbon cycle in these models because they may reflect differences in the process sensitivities to
540 drivers that are themselves climate sensitive.

541

542 In this study we expand on the framework proposed by Mongwe et al. (2016), which examined the
543 competing roles of temperature and DIC as drivers of pCO₂ variability and the seasonal cycle of pCO₂ in
544 the Southern Ocean, to explain the mechanistic basis for seasonal biases of pCO₂ and FCO₂ between
545 observational products and CMIP5 models. This analysis of 10 CMIP5 models and one observational
546 product (Landschutzer et al., 2014) highlighted that although the models showed different seasonal
547 cycles (Fig. 2), they could be grouped into two categories (SST- and DIC-driven) according to their
548 mean seasonal bias of temperature or DIC control (Fig. 3 & 6).

549
550 A few general insights emerge from this analysis. Firstly, despite significant differences in the spatial
551 characteristics of the mean annual fluxes (Fig. 1), models show unexpectedly greater inter-basin
552 coherence in the phasing seasonal cycle of FCO₂ and SST-DIC control than observational products (Fig.
553 3 & 6). Clear inter-basin differences have been highlighted in studies on the climatology and
554 interannual variability that examined pCO₂ and CO₂ fluxes based on data products (Landschutzer et al.,
555 2015; Gregor et al., 2017), as well as phytoplankton chlorophyll based on remote sensing (Thomalla et
556 al., 2011; Carranza et al., 2016). Briefly, the Atlantic basin shows the highest mean primary
557 production in contrast to the Pacific basin, which has the lowest (Thomalla et al., 2011). Similarly,
558 strong inter-basin differences for pCO₂ and FCO₂ have been highlighted and ascribed to SST control
559 (Landschützer et al., 2016) and wind stress - mixed layer depth (Gregor et al., 2017). The combined
560 effect of these regional differences in forcing of pCO₂ and FCO₂ would be expected to be reflected in the
561 CMIP5 models as well. A quantitative analysis of the correlation of the phasing of the seasonal cycle of
562 FCO₂ between basins for different models shows that all the models except three (CMCC-CESM, GFDL-
563 ESM2M CESM1-CESM) are characterized by strong inter-basin correlation in both the SAZ and the AZ
564 (Fig. 4). This suggests that the carbon cycle in these CMIP5 models is not sensitive to inter-basin
565 differences in the drivers as is the case for observations. This most likely implies that CMIP5 models
566 are not sensitive to regional FCO₂ variability at the basin scale, so FCO₂ seasonal biases are zonally
567 uniform.

568
569 Secondly, an important part of this analysis is based on the assumption that the observational
570 products that are used to constrain the spatial and temporal variability of pCO₂ and FCO₂ reflect the
571 correct seasonal cycles of the Southern Ocean. This assumption requires significant caution not only
572 due to the limitations in the sparseness of the *in situ* observations but also due to limitations of the
573 empirical techniques in overcoming these data gaps (Landschutzer et al., 2014; Rödenbeck et al., 2015;
574 Gregor et al., 2017a, b; Ritter et al., 2018). The uncertainty analysis from these studies suggests that,
575 while the seasonal bias in observations may be less in the SAZ and PFZ, it is the highest in the AZ
576 where access is limited mostly to summer, and winter ice cover results in uncertainties that may limit
577 the significance of the data-model comparisons. It is important to note that though the observation

578 product that we use here (Landschützer et al., (2014) is based on more surface measurement (10
579 millions, SOCAT v3) compared to previous datasets (e.g. Takahashi et al., 2009, 3 millions), the data
580 are still sparse in time and space in the Southern Ocean. Thus, in using this data product as our main
581 observational estimates for this analysis we are mindful of the limitations in the discussion below.

582
583 Thirdly, the seasonal cycle of $\Delta p\text{CO}_2$ is the dominant mode of variability in FCO_2 (Mongwe et al., 2016;
584 Wanninkhof et al., 2009). Though winds provide the kinematic forcing for air-sea fluxes of CO_2 and
585 indirectly affect FCO_2 through mixed layer dynamics and associated biogeochemical responses
586 (Mahadevan et al., 2012; du Plessis et al., 2017), $\Delta p\text{CO}_2$ sets the direction of the flux. Surface $p\text{CO}_2$
587 changes are mainly driven by DIC and SST (Hauck et al., 2015; Takahashi et al., 1993). Subsequently
588 the sensitivity of CMIP5 models to how changes in DIC and SST regulate the seasonal cycle of FCO_2 is
589 fundamental to the model's ability to resolve the observed FCO_2 seasonal cycle. Thus, here we
590 examined the influence of DIC and SST on FCO_2 at seasonal scale for 10 CMIP5 models with respect to
591 observed estimates. Because temperature does not directly affect DIC changes, we first scaled up the
592 impact of SST changes on $p\text{CO}_2$ through surface CO_2 solubility to equivalent DIC units using the Revelle
593 factor (section 2.3). In this way, we can distinguish the influence of surface solubility and DIC changes
594 (i.e. biological and physical) on $p\text{CO}_2$ and hence on FCO_2 .

595
596 Fourthly, using this analysis framework (sec 2.3, summarized in Fig. 6) we found that CMIP5 models
597 FCO_2 biases cluster in two groups, namely group-DIC ($M_{\text{T-DIC}} < 0$) and group-SST ($M_{\text{T-DIC}} > 0$). Group-DIC
598 models are characterized by an overestimation of the influence of DIC on $p\text{CO}_2$ with respect to
599 observations estimates, which instead indicate that physical and biogeochemical changes in the DIC
600 concentration mostly regulate the seasonal cycle of FCO_2 (in short, DIC control). Group-SST models
601 show an excessive temperature influence on $p\text{CO}_2$; here surface CO_2 solubility biases are mainly
602 responsible for the departure of modelled FCO_2 from the observational products. While CMIP5 models
603 mostly show a singular dominant influence of these extremes, observations show a modest influence
604 of both, with a dominance of DIC changes as the main driver of seasonal FCO_2 variability. Below we
605 discuss the seasonal cycle characteristics and possible mechanisms for these two groups of CMIP5
606 models in the Sub-Antarctic and Antarctic Zones of the Southern Ocean.

607

608 **4.1 Sub-Antarctic Zone (SAZ)**

609

610 Our diagnostic analysis indicates that the seasonal cycle of $p\text{CO}_2$ in the observational product
611 (Landschützer et al., 2014) is mostly DIC controlled across all three basins of the SAZ ($M_{\text{T-DIC}} < 0$ in Fig.
612 6). The Atlantic basin shows a stronger DIC control (Annual mean $M_{\text{T-DIC}} \geq 2$) compared to the Pacific
613 and Indian basin (Annual mean $M_{\text{T-DIC}} \approx 1$). This stronger influence of DIC on $p\text{CO}_2$ in the Atlantic basin

614 is consistent with higher primary production in this basin (Graham et al., 2015; Thomalla et al., 2011),
615 here shown by the larger mean seasonal chlorophyll from remote sensing in the Atlantic basin with
616 respect to the Pacific and Indian basin (Fig. 8). This significant basin difference is most likely linked to
617 the fact that the Atlantic basin has longer periods of shallow MLD compared to the Pacific and Indian
618 basins (Fig. 7a-c, Nov – Mar & Nov - Feb respectively) and has been shown to have higher supplies of
619 continental shelves and land-based iron (Boyd and Ellwood, 2010; Tagliabue et al., 2012; 2014). These
620 conditions are more likely to enhance primary production that translates into a higher rate of change
621 of surface DIC (Fig. 8), which becomes the major driver of FCO_2 variability. In contrast, shorter periods
622 of shallow MLD and lower iron inputs in the Pacific basin (Tagliabue et al., 2012), likely account for a
623 lower chlorophyll biomass and hence the weaker DIC control evidenced in our analysis ($M_{T-DIC} \approx 0$ in
624 Fig. 6). In the Indian basin, the winter mixed layer is deeper than in the Atlantic and deepens earlier in
625 the season (Fig. 7c). These conditions limit chlorophyll concentration (Fig. 8) and possibly contribute
626 to the lower rates of surface temperature change because of the enhanced mixing (cf Fig. 5a-c). As a
627 consequence, the resulting net driver in the Indian and Pacific basins is a weaker DIC control, because
628 both biological DIC and solubility changes are relatively weaker and they oppose each other. Because
629 of this, when the magnitudes of the rate of change of SST are larger during cooling and warming
630 seasonal peaks (autumn and spring respectively), DIC control is weaker ($M_{T-DIC} \approx 0$) during these
631 seasons.

632
633 CMIP5 models do not capture these basin-specific features as demonstrated with the correlation
634 analysis in Fig. 4, with the exception of three group-SST models (i.e. CESM1-BGC, GFDL-ESM2M and
635 CMCC-CESM). These, in contrast, mostly show comparable FCO_2 phasing in the three basins. The
636 seasonal cycle of CO_2 flux in the Southern Ocean (3,4) is both zonally and meridionally uniform for
637 most CMIP5 models, in contrast to observational data product (Fig. 3). This suggests that CMIP5
638 models show equal sensitivity to basin scale FCO_2 drivers, suggesting that pCO_2 and FCO_2 driving
639 mechanisms are less local than for observations. Thus the understanding of fine-scale (mesoscale and
640 sub-mesoscale) processes responsible for basin-scale FCO_2 variability will be an important
641 contribution to the next generation of ESM. Studies based on new available data from higher
642 resolution autonomous platforms like Monteiro et al., (2015), Williams et al., (2017). Briggs et al.,
643 (2018) and Rosso et al., (2017) may be useful constraints to these dynamics in ESMs.

644
645 The major feature of group-SST models in the SAZ is the out-gassing during summer and in-gassing
646 mid-autumn to winter (Fig. 3a-c, Apr-Aug), which our diagnostics in Fig. 6 attribute to temperature
647 (solubility) control. The summer period coincides with the highest warming rates ($dSST/dt$, Fig 5a-c),
648 and associated reduction in solubility of CO_2 . Similarly, exaggerated cooling rates at the onset of
649 autumn (Fig. 5a-c) enhance CO_2 solubility causing a change in the direction of FCO_2 into strengthening

650 CO₂ in-gassing (Fig 3a-c). Thus, while group-SST models have a seasonal amplitude of FCO₂
651 comparable to observations, they are out of phase (Fig. 3) as was the case in a previous analysis of a
652 forced ocean model (Mongwe et al., 2016).

653
654 In addition to increasing CO₂ solubility, the rapid cooling at the onset of autumn also deepens the MLD
655 (March-June, Fig. 7), which induces entrainment of DIC, increasing surface CO₂ concentration and
656 weakening the ocean-atmosphere gradient, and, in some instances, reversing the air-sea flux to out-
657 gassing (Lenton et al., 2013a; Mahadevan et al., 2011; Metzl et al., 2006). While these processes
658 (cooling and DIC entrainment) are likely to co-occur in the Southern Ocean, in CMIP5 models they are
659 characterized by their extremes: temperature impact of solubility exceeds the rate of entrainment
660 (Fig. 6 & 10). Because of the dominance of the solubility effect in group-SST models, the impact of DIC
661 entrainment on surface pCO₂ changes, the weakening of CO₂ in-gassing / out-gassing only happens in
662 mid-late winter (June-July -August) when entrainment fluxes peak (Fig. 10) and the SST rate
663 approaches zero (Fig. 5).

664
665 In the spring-summer transition, primary production is expected to enhance the net CO₂ uptake
666 (Thomalla et al., 2011; Le Quéré and Saltzman, 2013). However, the elevated surface warming rates
667 during spring reduces CO₂ solubility in group-SST models and overwhelms the role of primary
668 production in the seasonal cycle of pCO₂ and FCO₂ (atmospheric CO₂ uptake). As a consequence, these
669 group-SST models mostly show a constant or weakening net CO₂ uptake flux during spring in the
670 Pacific and Atlantic basin even though primary production is occurring and is relatively elevated (Fig.
671 3 & 8). Though some models show chlorophyll concentrations comparable to observations (e.g. GFDL-
672 ESM2M, CNRM-CM5, CanESM2), and sometimes greater (e.g. MRI-ESM), the impact of temperature-
673 driven solubility still dominates due to the phasing of the rates of the two drivers (Fig. 2a-c). The
674 Indian basin however shows the only exception to this phenomenon. Here, the amplitude of the
675 seasonal surface warming is relatively smaller (~ 0.5 °C⁻¹ month⁻¹ lower than the Pacific and Atlantic
676 basins), and the biologically-driven CO₂ uptake becomes notable and shows a net strengthening of the
677 sink of CO₂ during spring (Fig. 3c).

678
679 Though almost all analyzed CMIP5 models (with the exception of NorESM1-ME) exaggerate the
680 warming and cooling rates in autumn and spring, group-DIC models do not manifest the expected
681 temperature-driven solubility impact on pCO₂ and FCO₂ (Fig. 2). Instead, the seasonal cycle of pCO₂ and
682 FCO₂ are controlled by DIC changes, which are driven by an overestimated seasonal primary
683 production and the associated export carbon (Fig. 8). It is striking how in these models the seasonal
684 cycle of chlorophyll and FCO₂ are in phase (Fig 3a-c, 8a-c, with linear correlation coefficients always

685 larger than 0.9 not shown) but, as we discuss below, this is not because the temperature rates of
686 change are correctly scaled but because the biogeochemical process rates are exaggerated (Fig. 8).

687

688 Because of the particularly enhanced production in group-DIC models, the CO₂ sink is stronger (Fig. 8)
689 with respect to observation estimates during spring. This is visible in the reduction of surface DIC
690 (negative dDIC/dt in Fig. 8a, g-i), which can only be explained by drawdown due to the formation and
691 export of organic matter (Le Quéré and Saltzman, 2013). However, note that in the same way, after the
692 December production peak, both CMIP5 models and observations show an increase of surface DIC
693 concentrations (positive dDIC/dt) until March (Fig. 8, g-i). These DIC growth rates are particularly
694 enhanced in group-DIC models compared to some group-SST and observations (Fig. S9). The onset of
695 these DIC increases also coincides with the depletion of surface oxygen (Fig. S9), which we speculate is
696 due to the remineralization of organic matter to DIC through respiration. Unfortunately, only a few
697 models have stored the respiration rates, therefore the full reason for this DIC rebound remains to be
698 examined at a later stage. We would however tend to exclude other processes, because the onset of
699 CO₂ out-gassing seen in March in group-DIC models occurs prior to significant MLD deepening (Fig. 7)
700 and entrainment fluxes, therefore remineralization is likely be a key process here (Fig. 8).

701

702 **4.2 Antarctic Zone (AZ)**

703

704 The seasonal cycle framework summarized in Fig. 6 shows that the variability of FCO₂ and pCO₂ in the
705 Landschützer et al. (2014) product is characterized by a stronger DIC control (annual mean $M_{T-DIC} < -2$)
706 relative to the Sub-Antarctic ($M_{T-DIC} \approx -1$), except in the spring season ($M_{T-DIC} > -1$). This DIC control is
707 spatially uniform in the Antarctic Zone across all three basins (Fig. 4). The available datasets indicate
708 that the combination of weaker SST rates due to lower solar heating fluxes (Fig. 5), and stronger
709 shallower vertical DIC maxima (Fig. 10) favour a stronger DIC control through larger surface DIC rates.
710 The spatial uniformity in the seasonality of FCO₂ is also evident in the satellite chlorophyll and
711 calculated dDIC/dt from GLODAP2 in Fig. 9. Contrary to the Sub-Antarctic this might be suggesting
712 that FCO₂ mechanisms here are less local. It could be hypothesized that the seasonal extent of sea-ice,
713 deeper mixing and heat balance differences affect this region more uniformly compared to the Sub-
714 Antarctic Zone, and hence the mechanisms of FCO₂ are spatially homogeneous. However, we cannot
715 forget that sparseness of observations in this region is a key limitation to data products (Bakker et al.,
716 2014; Gregor et al., 2017; Monteiro et al., 2010; Rödenbeck et al., 2013) that might hamper the
717 emergence of basin-specific features. Consequently, this highlights the importance and need to
718 prioritize independent observations in the Southern Ocean south of the polar front and in the Marginal
719 Ice Zone. Increased observational efforts should also include a variety of platforms such as

720 autonomous vehicles like gliders (Monteiro et al., 2015) and biogeochemical floats (Johnson et al.,
721 2017) in addition to ongoing ship-based measurements.

722

723 In general terms, CMIP5 models are mostly in agreement (with an exception of MRI-ESM) with the
724 observational product on the dominant role of DIC to regulating the seasonal cycle of FCO₂ (Fig. 6d-f),
725 though not all models agree in the phase of the seasonal cycle of FCO₂ (e.g. CanESM2, Fig. 2). Though
726 CMIP5 models still mostly show the SST rates biases in autumn and spring with respect to observed
727 estimates, the stronger and near-surface vertical DIC maxima (Fig. 10), likely favor DIC as a dominant
728 driver of FCO₂ changes. Differences between group-SST and group-DIC models are only evident in mid-
729 summer when SST rates heighten and primary production peaks (Fig. 3 & 9). Probably because of sea
730 ice presence, the onset of SST warming is a month later (November) here in comparison to the Sub-
731 Antarctic (October). This subsequently allows the onset of primary production before the surface
732 warming, which then permits the biological CO₂ uptake to be notable in group-SST models. Thus the
733 two model groups here agree in the FCO₂ in-gassing during spring with group-SST models being the
734 closest to the observational product. The MRI-ESM is the only model showing anomalous solubility
735 dominance during autumn and spring as in the Sub-Antarctic Zone.

736

737 This coherence of CMIP5 models and observations in the Antarctic Zone may suggest that CMIP5
738 models compare better to observations in this region (Fig. 4). However, because CMIP5 models also
739 show this spatial homogeneity in the Sub-Antarctic Zone (contrary to observational estimates), it is
740 not clear whether this indicates an improved skill in CMIP5 model to the mechanisms of FCO₂ in this
741 region, or both CMIP5 models and observational product lacks spatial sensitivity to the drivers of
742 FCO₂. The sparseness of observations in the AZ points to the latter.

743

744 The cause of differences in the seasonal rates of SST change in group-SST models remains a subject of
745 ongoing research. The Southern Ocean is a part of the global ocean (upwelling) where earth systems
746 models show a persistent warming SST bias (Hirahara et al., 2014). Several studies point to highlight
747 potential explanations but the main reasons remains uncertain. For example, CMIP5 models
748 differences in the magnitude and meridional location of the peak of wind speeds in the Southern Ocean
749 (Bracegirdle et al., 2013) and MLD differences (Meijers, 2014; Sallée et al., 2013) may be such that the
750 net effect of change on surface turbulence and mixing leads to these amplified surface temperature
751 rates. Other known CMIP5 models' biases that which may contribute includes; heat fluxes and storage
752 (Frölicher et al., 2015) as well as sea-ice dynamics (Turner et al., 2013). Notwithstanding these,
753 investigation of the reasons for sources of these dSST/dt biases is out of the scope of this study. Our
754 aim here is to show that understanding biases in the drivers of pCO₂ (DIC and SST) at the seasonal
755 scale is necessary to understand differences in the seasonal cycle of FCO₂ between models and

756 observational products. However we recommend that the mechanistic basis for the differences the
757 seasonal rates of warming and cooling be a matter of urgent investigated further

758 .

759

760

761

762

763 **5. Synthesis**

764

765 We used a seasonal cycle framework to highlight and examine two major biases in respect of pCO₂ and
766 FCO₂ in 10 CMIP5 models in the Southern Ocean.

767

768 Firstly, we examined the general exaggeration of the seasonal rates of change of SST in autumn and
769 spring seasons during peak cooling and warming respectively with respect to available observations.
770 These elevated rates of SST change tip the control of the seasonal cycle of pCO₂ and FCO₂ towards SST
771 from DIC and result in a divergence between the observed and modelled seasonal cycles, particularly
772 in the Sub-Antarctic Zone. While almost all analyzed models (9 of 10) show these SST-driven biases, 3
773 of the 10 (namely NorESM1-ME, HadGEM-ES and MPI-ESM) don't show these solubility biases because
774 of their overly exaggerated primary production (and remineralization) rates such that biologically-
775 driven DIC changes mainly regulate the seasonal cycle of FCO₂. These models reproduce the observed
776 phasing of FCO₂ as a result of an incorrect scaling of the biogeochemical fluxes. In the Antarctic Zone,
777 CMIP5 models compare better with observations relative to the Sub-Antarctic Zone. This is mostly
778 because both CMIP5 models and observational product estimates show a spatial and temporal
779 uniformity in the characteristics of FCO₂ in the Antarctic Zone. However, it is not certain if this is
780 because model process dynamics perform better in this high latitude zone or that the observational
781 products variability is itself limited by the lack of *in situ data*. This remains an open question that
782 needs to be explored further and highlights the need for increased scale-sensitive and independent
783 observations south of the Polar Front and into the sea-ice zone.

784

785 The second major bias is that contrary to observational products estimates, CMIP5 models generally
786 show an equal sensitivity to basin scale FCO₂ drivers (except for CMCC-ESM, GFDL-ESM2M and
787 CESM1-BGC) and hence the seasonal cycle of FCO₂ has similar phasing in all three basins of the Sub-
788 Antarctic Zone. This is in contrast to observational and remote sensing products that highlight strong
789 seasonal and interannually varying basin contrasts in both pCO₂ and phytoplankton biomass. It is not
790 clear if this is due to inadequate carbon process parameterization or improper representation of the

791 dynamics of the physics. This should be investigated further with CMIP6 models and our analysis
792 framework is proposed as a useful tool to diagnose the dominant drivers. Contrary to observed
793 estimates, CMIP5 models simulate FCO₂ seasonal dynamics that are zonally homogeneous and we
794 suggest that any investigation of local (basin-scale) mechanisms, dynamics and long term trends of
795 FCO₂ using CMIP5 models must remain tentative and should be treated with caution. This highlights a
796 key area of development for the next generation of models such those planned to be used for CMIP6.
797

798

799

800 **Acknowledgements**

801

802 This work was undertaken with financial support from the following South African institutions: CSIR
803 Parliamentary Grant, National Research Foundation (NRF SANAP programme), Department of Science
804 and Technology South Africa (DST), and the Applied Centre for Climate and Earth Systems Science
805 (ACCESS). We thank the CSIR Centre for High Performance Computing (CHPC) for providing the
806 resources for doing this analysis. We also want to thank Peter Landschützer, Taro Takahashi and Luke
807 Gregor for making their data products available as well as the three reviewers for their productive
808 comments that we think have strengthened the paper

809

810 **References**

811

812 Anav, A., Friedlingstein, P., Kidston, M., Bopp, L., Ciais, P., Cox, P., Jones, C., Jung, M., Myneni, R. and Zhu,
813 Z.: Evaluating the land and ocean components of the global carbon cycle in the CMIP5 earth system
814 models, *J. Clim.*, 26(18), 6801–6843, doi:10.1175/JCLI-D-12-00417.1, 2013.

815

816 Bakker, D. C. E., Pfeil, B., Smith, K., Hankin, S., Olsen, A., Alin, S. R., Cosca, C., Harasawa, S., Kozyr, A.,
817 Nojiri, Y., O'Brien, K. M., Schuster, U., Telszewski, M., Tilbrook, B., Wada, C., Akl, J., Barbero, L., Bates, N.
818 R., Boutin, J., Bozec, Y., Cai, W.-J., Castle, R. D., Chavez, F. P., Chen, L., Chierici, M., Currie, K., De Baar, H. J.
819 W., Evans, W., Feely, R. A., Fransson, A., Gao, Z., Hales, B., Hardman-Mountford, N. J., Hoppema, M.,
820 Huang, W.-J., Hunt, C. W., Huss, B., Ichikawa, T., Johannessen, T., Jones, E. M., Jones, S. D., Jutterström, S.,
821 Kitidis, V., Körtzinger, A., Landschützer, P., Lauvset, S. K., Lefèvre, N., Manke, A. B., Mathis, J. T., Merlivat,
822 L., Metzl, N., Murata, A., Newberger, T., Omar, A. M., Ono, T., Park, G.-H., Paterson, K., Pierrot, D., Ríos, A.
823 F., Sabine, C. L., Saito, S., Salisbury, J., Sarma, V. V. S. S., Schlitzer, R., Sieger, R., Skjelvan, I., Steinhoff, T.,

824 Sullivan, K. F., Sun, H., Sutton, A. J., Suzuki, T., Sweeney, C., Takahashi, T., Tjiputra, J. F., Tsurushima, N.,
825 Van Heuven, S. M. A. C., Vandemark, D., Vlahos, P., Wallace, D. W. R., Wanninkhof, R. H. and Watson, A.
826 J.: An update to the surface ocean CO₂ atlas (SOCAT version 2), *Earth Syst. Sci. Data*, 6(1), 69–90,
827 doi:10.5194/essd-6-69-2014, 2014.

828

829 Barbero, L., Boutin, J., Merlivat, L., Martin, N., Takahashi, T., Sutherland, S. C. and Wanninkhof, R.:
830 Importance of water mass formation regions for the air-sea CO₂ flux estimate in the southern ocean,
831 *Global Biogeochem. Cycles*, 25(1), 1–16, doi:10.1029/2010GB003818, 2011.

832

833 Boyd, P. W. and Ellwood, M. J.: The biogeochemical cycle of iron in the ocean, *Nat. Geosci.*, 3(10), 675–
834 682, doi:10.1038/ngeo964, 2010.

835

836 Bracegirdle, T. J., Shuckburgh, E., Sallee, J. B., Wang, Z., Meijers, A. J. S., Bruneau, N., Phillips, T.
837 and Wilcox, L. J.: Assessment of surface winds over the atlantic, indian, and pacific ocean
838 sectors of the southern ocean in cmip5 models: Historical bias, forcing response, and state
839 dependence, *J. Geophys. Res. Atmos.*, 118(2), 547–562, doi:10.1002/jgrd.50153, 2013.

840

841 de Boyer Montégut, C., Madec, G., Fischer, A. S., Lazar, A. and Iudicone, D.: Mixed layer depth over the
842 global ocean: An examination of profile data and a profile-based climatology, *J. Geophys. Res. C Ocean.*,
843 109(12), 1–20, doi:10.1029/2004JC002378, 2004.

844

845 Dickson, A. G. and Millero, F. J.: A comparison of the equilibrium constants for the dissociation of
846 carbonic acid in seawater media, *Deep Sea Res. Part A, Oceanogr. Res. Pap.*, 34(10), 1733–1743,
847 doi:10.1016/0198-0149(87)90021-5, 1987.

848

849 Dufour, C. O., Sommer, J. Le, Gehlen, M., Orr, J. C., Molines, J. M., Simeon, J. and Barnier, B.: Eddy
850 compensation and controls of the enhanced sea-to-air CO₂ flux during positive phases of the Southern
851 Annular Mode, *Global Biogeochem. Cycles*, 27(3), 950–961, doi:10.1002/gbc.20090, 2013.

852

853 Feely, R. A., Wanninkhof, R., McGillis, W., Carr M. E and Cosca, C.: Effects of wind speed and gas
854 exchange parameterizations on the air-sea CO₂ fluxes in the equatorial Pacific Ocean, *J. Geophys. Res.*,
855 109(C8), C08S03, doi:10.1029/2003JC001896, 2004.

856

857 Frölicher, T. L., Sarmiento, J. L., Paynter, D. J., Dunne, J. P., Krasting, J. P. and Winton, M.: Dominance of
858 the Southern Ocean in anthropogenic carbon and heat uptake in CMIP5 models, *J. Clim.*, 28(2), 862–
859 886, doi:10.1175/JCLI-D-14-00117.1, 2015.

860
861 Fung, I. Y., Doney, S. C., Lindsay, K. and John, J.: Evolution of carbon sinks in a changing climate, Proc.
862 Natl. Acad. Sci., 102(32), 11201–11206, doi:10.1073/pnas.0504949102, 2005.
863
864 Graham, R. M., De Boer, A. M., van Sebille, E., Kohfeld, K. E. and Schlosser, C.: Inferring source regions
865 and supply mechanisms of iron in the Southern Ocean from satellite chlorophyll data, Deep. Res. Part I
866 Oceanogr. Res. Pap., 104, 9–25, doi:10.1016/j.dsr.2015.05.007, 2015.
867
868 Gregor, L., Kok, S. and Monteiro, P. M. S.: Empirical methods for the estimation of Southern Ocean CO₂:
869 support vector and random forest regression, Biogeosciences, 14(23), 5551–5569, doi:10.5194/bg-14-
870 5551-2017, 2017a.
871
872 Gregor, L., Kok, S. and Monteiro, P. M. S.: Interannual drivers of the seasonal cycle of CO₂ fluxes in the
873 Southern Ocean, Biogeosciences Discuss., (September), 1–28, doi:10.5194/bg-2017-363, 2017b.
874
875 Gruber, N., Gloor, M., Mikaloff Fletcher, S. E., Doney, S. C., Dutkiewicz, S., Follows, M. J., Gerber, M.,
876 Jacobson, A. R., Joos, F., Lindsay, K., Menemenlis, D., Mouchet, A., Müller, S. A., Sarmiento, J. L. and
877 Takahashi, T.: Oceanic sources, sinks, and transport of atmospheric CO₂, Global Biogeochem. Cycles,
878 23(1), 1–21, doi:10.1029/2008GB003349, 2009.
879
880 Hauck, J. and Völker, C.: A multi-model study on the Southern Ocean CO₂ uptake and the role of the
881 biological carbon pump in the 21st century, EGU Gen. Assem., 17, 12225,
882 doi:10.1002/2015GB005140.Received, 2015.
883
884 Hauck, J., Völker, C., Wolf-Gladrow, D. a., Laufkötter, C., Vogt, M., Aumont, O., Bopp, L., Buitenhuis, E. T.,
885 Doney, S. C., Dunne, J., Gruber, N., John, J., Le Quéré, C., Lima, I. D., Nakano, H. and Totterdell, I.: On the
886 Southern Ocean CO₂ uptake and the role of the biological carbon pump in the 21st century, Global
887 Biogeochem. Cycles, 29, 1451–1470, doi:10.1002/2015GB005140, 2015.
888
889 Hirahara, S., Ishii, M. and Fukuda, Y.: Centennial-scale sea surface temperature analysis and its
890 uncertainty, J. Clim., 27(1), 57–75, doi:10.1175/JCLI-D-12-00837.1, 2014.
891
892 Ilyina, T., Six, K. D., Segschneider, J., Maier-Reimer, E., Li, H. and Núñez-Riboni, I.: Global ocean
893 biogeochemistry model HAMOCC: Model architecture and performance as component of the MPI-Earth
894 system model in different CMIP5 experimental realizations, J. Adv. Model. Earth Syst., 5(2), 287–315,
895 doi:10.1029/2012MS000178, 2013.

896
897 Johnson, K. S., Plant, J. N., Coletti, L. J., Jannasch, H. W., Sakamoto, C. M., Riser, S. C., Swift, D. D., Williams,
898 N. L., Boss, E., Haëntjens, N., Talley, L. D. and Sarmiento, J. L.: Biogeochemical sensor performance in
899 the SOCCOM profiling float array, *J. Geophys. Res. Ocean.*, (September), doi:10.1002/2017JC012838,
900 2017.
901
902 Johnson, R., Stratton, P. G., Wright, S. W., McMinn, A. and Meiners, K. M.: Three improved satellite
903 chlorophyll algorithms for the Southern Ocean, *J. Geophys. Res. Ocean.*, 118(7), 3694–3703,
904 doi:10.1002/jgrc.20270, 2013.
905
906 Kessler, A. and Tjiputra, J.: The Southern Ocean as a constraint to reduce uncertainty in future ocean
907 carbon sinks, *Earth Syst. Dyn.*, 7(2), 295–312, doi:10.5194/esd-7-295-2016, 2016.
908
909 Landschützer, P., Gruber, N. and Bakker, D. C. E. Stemmler, I. and Six, K. D.: Strengthening seasonal
910 marine CO₂ variations due to increasing atmospheric CO₂. *Nature Climate Change*, 8, 146-150, Doi:
911 10.1038/s41558-017-0057-x, 2018.
912
913 Landschützer, P., Gruber, N. and Bakker, D. C. E.: Decadal variations and trends of the global ocean
914 carbon sink, *Global Biogeochem. Cycles*, 30(10), 1396–1417, doi:10.1002/2015GB005359, 2016.
915
916 Landschützer, P., Gruber, N., Haumann, F. A., Rodenbeck, C., Bakker, D. C. E., van Heuven, S., Hoppema,
917 M., Metzl, N., Sweeney, C., Takahashi, T., Tilbrook, B. and Wanninkhof, R.: The reinvigoration of the
918 Southern Ocean carbon sink, *Science (80-.)*, 349(6253), 1221–1224, doi:10.1126/science.aab2620,
919 2015.
920
921 Landschützer, P., Gruber, N., Bakker, D. C. E. and Schuster, U.: Recent variability of the global ocean
922 carbon sink, *Glob. Planet. Change*, 927–949, doi:10.1002/2014GB004853. Received, 2014.
923
924 Landschützer, P., Gruber, N., Bakker, D. C. E., Schuster, U., Nakaoka, S., Payne, M. R., Sasse, T. P. and
925 Zeng, J.: A neural network-based estimate of the seasonal to inter-annual variability of the Atlantic
926 Ocean carbon sink, *Biogeosciences*, 10(11), 7793–7815, doi:10.5194/bg-10-7793-2013, 2013.
927
928 Lauvset, S. K., Key, R. M., Olsen, A., Van Heuven, S., Velo, A., Lin, X., Schirnick, C., Kozyr, A., Tanhua, T.,
929 Hoppema, M., Jutterström, S., Steinfeldt, R., Jeansson, E., Ishii, M., Perez, F. F., Suzuki, T. and Watelet, S.:
930 A new global interior ocean mapped climatology: The 1° × 1° GLODAP version 2, *Earth Syst. Sci. Data*,
931 8(2), 325–340, doi:10.5194/essd-8-325-2016, 2016.

932

933 Lee, K., Tong, L. T., Millero, F. J., Sabine, C. L., Dickson, A. G., Goyet, C., Park, G. H., Wanninkhof, R., Feely,
 934 R. A. and Key, R. M.: Global relationships of total alkalinity with salinity and temperature in surface
 935 waters of the world's oceans, *Geophys. Res. Lett.*, 33(19), 1–5, doi:10.1029/2006GL027207, 2006.

936

937 Lenton, A., Metzl, N., Takahashi, T., Kuchinke, M., Matear, R. J., Roy, T., Sutherland, S. C., Sweeney, C. and
 938 Tilbrook, B.: The observed evolution of oceanic pCO₂ and its drivers over the last two decades, *Global*
 939 *Biogeochem. Cycles*, 26(2), 1–14, doi:10.1029/2011GB004095, 2012.

940

941 Lenton, A., Tilbrook, B., Law, R., Bakker, D., Doney, S. C., Gruber, N., Hoppema, M., Ishii, M., Lovenduski,
 942 N. S., Matear, R. J., McNeil, B. I., Metzl, N., Mikaloff Fletcher, S. E., Monteiro, P., Rödenbeck, C., Sweeney,
 943 C. and Takahashi, T.: Sea-air CO₂ fluxes in the Southern Ocean for the period
 944 1990–2009, *Biogeosciences Discuss.*, 10(1), 285–333, doi:10.5194/bgd-10-285-2013,
 945 2013.

946

947 Leung, S., Cabre, A. and Marinov, I.: A latitudinally banded phytoplankton response to 21st century
 948 climate change in the Southern Ocean across the CMIP5 model suite, *Biogeosciences*, 12(19), 5715–
 949 5734, doi:10.5194/bg-12-5715-2015, 2015.

950

951 Locarnini, R. A., Mishonov, A. V., Antonov, J. I., Boyer, T. P., Garcia, H. E., Baranova, O. K., Zweng, M. M.,
 952 Paver, C. R., Reagan, J. R., Johnson, D. R., Hamilton, M. and Seidov, D.: *World Ocean Atlas 2013. Vol. 1:*
 953 *Temperature.*, 2013.

954

955 Mahadevan, A., Tagliabue, A., Bopp, L., Lenton, A., Memery, L. and Levy, M.: Impact of episodic vertical
 956 fluxes on sea surface pCO₂, *Philos. Trans. R. Soc. A Math. Phys. Eng. Sci.*, 369(1943), 2009–2025,
 957 doi:10.1098/rsta.2010.0340, 2011.

958

959 Mahadevan, A., D'Asaro, E., Lee, C. and Perry, M. J.: Eddy-driven stratification initiates North Atlantic
 960 spring phytoplankton blooms, *Science* (80-.), 336(6090), 54–58, doi:10.1126/science.1218740, 2012.

961 Marinov, I. and Gnanadesikan, A.: Changes in ocean circulation and carbon storage are decoupled from
 962 air-sea CO₂ fluxes, *Biogeosciences*, 8(2), 505–513, doi:10.5194/bg-8-505-2011, 2011.

963

964 Marinov, I., Gnanadesikan, A., Toggweiler, J. R. and Sarmiento, J. L.: The Southern Ocean
 965 biogeochemical divide, *Nature*, 441(7096), 964–967, doi:10.1038/nature04883, 2006.

966

967 Matear, R. J. and Lenton, A.: Impact of Historical Climate Change on the Southern Ocean Carbon Cycle, *J.*

968 Clim., 21(22), 5820–5834, doi:10.1175/2008JCLI2194.1, 2008.
969
970 McNeil, B. I., Metzl, N., Key, R. M., Matear, R. J. and Corbiere, A.: An empirical estimate of the Southern
971 Ocean air-sea CO₂ flux, *Global Biogeochem. Cycles*, 21(3), 1–16, doi:10.1029/2007GB002991, 2007.
972
973 Mehrbach, C., Culberson, C. H., Hawley, J. E. and Pytkowicz, R. M.: Measurement of the Apparent
974 Dissociation Constants of Carbonic Acid in Seawater At Atmospheric Pressure, *Limnol. Oceanogr.*,
975 18(6), 897–907, doi:10.4319/lo.1973.18.6.0897, 1973.
976
977 Metzl, N.: Decadal increase of oceanic carbon dioxide in Southern Indian Ocean surface waters (1991-
978 2007), *Deep. Res. Part II Top. Stud. Oceanogr.*, 56(8–10), 607–619, doi:10.1016/j.dsr2.2008.12.007,
979 2009.
980 Metzl, N., Brunet, C., Jabaud-Jan, A., Poisson, A. and Schauer, B.: Summer and winter air-sea CO₂ fluxes
981 in the Southern Ocean, *Deep. Res. Part I Oceanogr. Res. Pap.*, 53(9), 1548–1563,
982 doi:10.1016/j.dsr.2006.07.006, 2006.
983
984 Mongwe, N. P., Chang, N. and Monteiro, P. M. S.: The seasonal cycle as a mode to diagnose biases in
985 modelled CO₂ fluxes in the Southern Ocean, *Ocean Model.*, 106, 90–103,
986 doi:10.1016/j.ocemod.2016.09.006, 2016.
987
988 Monteiro, P. M. S., et al. (2010), A global sea surface carbon observing system: Assessment of changing
989 sea surface CO₂ and air-sea CO₂ fluxes, in *Proceedings of the “OceanObs’09: Sustained Ocean
990 Observations and Information for Society” Conference*, edited by J. Hall, D. E. Harrison,
991 and D. Stammer, ESA Publ. WPP-306, Venice, Italy, doi:10.5270/OceanObs09.cwp.64, 21–25 Sept..
992
993 Monteiro, P. M. S., Gregor, L., Lévy, M., Maenner, S., Sabine, C. L. and Swart, S.: Intra-seasonal variability
994 linked to sampling alias in air – sea CO₂ fluxes in the Southern Ocean, *Geophys. Res. Lett.*, 1–8,
995 doi:10.1002/2015GL066009, 2015.
996
997 Moore, J. K., Doney, S. C. and Lindsay, K.: Upper ocean ecosystem dynamics and iron cycling in a global
998 three-dimensional model, *Global Biogeochem. Cycles*, 18(4), 1–21, doi:10.1029/2004GB002220, 2004.
999
1000 Orsi, A. H., Whitworth, T. and Nowlin, W. D.: On the meridional extent and fronts of the Antarctic
1001 Circumpolar Current, *Deep. Res. Part I*, 42(5), 641–673, doi:10.1016/0967-0637(95)00021-W, 1995.
1002
1003 Pasquer, B., Metzl, N., Goosse, H. and Lancelot, C.: What drives the seasonality of air-sea CO₂ fluxes in

L004 the ice-free zone of the Southern Ocean: A 1D coupled physical-biogeochemical model approach, *Mar.*
L005 *Chem.*, 177, 554–565, doi:10.1016/j.marchem.2015.08.008, 2015.

L006

L007 Pierrot, D. E. Lewis, and D. W. R. Wallace. 2006. MS Excel Program Developed for CO₂ System
L008 Calculations. ORNL/CDIAC-105a. Carbon Dioxide Information Analysis Center, Oak Ridge National
L009 Laboratory, U.S. Department of Energy, Oak Ridge, Tennessee. doi:
L010 10.3334/CDIAC/otg.CO2SYS_XLS_CDIAC105a

L011

L012 du Plessis, M., Swart, S., Ansong, I. J. and Mahadevan, A.: Submesoscale processes promote seasonal
L013 restratification in the Subantarctic Ocean, *J. Geophys. Res. Ocean.*, 122(4), 2960–2975,
L014 doi:10.1002/2016JC012494, 2017.

L015

L016 Le Quéré, C. and Saltzman, E. S.: *Surface Ocean-Lower Atmosphere Processes*, 2013.

L017 Le Quéré, C., Rödenbeck, C., Buitenhuis, E. T., Conway, T. J., Langenfelds, R., Gomez, A., Labuschagne, C.,
L018 Ramonet, M., Nakazawa, T., Metz, N., Gillett, N. and Heimann, M.: Saturation of the southern ocean CO₂
L019 sink due to recent climate change, *Science* (80-.), 316(5832), 1735–1738,
L020 doi:10.1126/science.1136188, 2007.

L021

L022 Le Quéré, C., Andrew, R. M., Canadell, J. G., Sitch, S., Ivar Korsbakken, J., Peters, G. P., Manning, A. C.,
L023 Boden, T. A., Tans, P. P., Houghton, R. A., Keeling, R. F., Alin, S., Andrews, O. D., Anthoni, P., Barbero, L.,
L024 Bopp, L., Chevallier, F., Chini, L. P., Ciais, P., Currie, K., Delire, C., Doney, S. C., Friedlingstein, P.,
L025 Gkritzalis, T., Harris, I., Hauck, J., Haverd, V., Hoppema, M., Klein Goldewijk, K., Jain, A. K., Kato, E.,
L026 Körtzinger, A., Landschützer, P., Lefèvre, N., Lenton, A., Lienert, S., Lombardozzi, D., Melton, J. R., Metz,
L027 N., Millero, F., Monteiro, P. M. S., Munro, D. R., Nabel, J. E. M. S., Nakaoka, S. I., O'Brien, K., Olsen, A.,
L028 Omar, A. M., Ono, T., Pierrot, D., Poulter, B., Rödenbeck, C., Salisbury, J., Schuster, U., Schwinger, J.,
L029 Séférian, R., Skjelvan, I., Stocker, B. D., Sutton, A. J., Takahashi, T., Tian, H., Tilbrook, B., Van Der Laan-
L030 Luijkx, I. T., Van Der Werf, G. R., Viovy, N., Walker, A. P., Wiltshire, A. J. and Zaehle, S.: Global Carbon
L031 Budget 2016, *Earth Syst. Sci. Data*, 8(2), 605–649, doi:10.5194/essd-8-605-2016, 2016.

L032

L033 Ritter, R., Landschützer, P., Gruber, N., Fay, A. R., Iida, Y., Jones, S., Nakaoka, S., Park, G. H., Peylin, P.,
L034 Rödenbeck, C., Rodgers, K. B., Shutler, J. D. and Zeng, J.: Observation-Based Trends of the Southern
L035 Ocean Carbon Sink, *Geophys. Res. Lett.*, doi:10.1002/2017GL074837, 2017.

L036

L037 Rödenbeck, C., Keeling, R. F., Bakker, D. C. E., Metz, N., Olsen, A., Sabine, C. and Heimann, M.: Global
L038 surface-ocean pCO₂ and sea-air CO₂ flux variability from an observation-driven ocean mixed-layer
L039 scheme, *Ocean Sci.*, 9(2), 193–216, doi:10.5194/os-9-193-2013, 2013.

L040
L041 Rodgers, K. B., Aumont, O., Mikaloff Fletcher, S. E., Plancherel, Y., Bopp, L., De Boyer Montégut, C.,
L042 Iudicone, D., Keeling, R. F., Madec, G. and Wanninkhof, R.: Strong sensitivity of Southern Ocean carbon
L043 uptake and nutrient cycling to wind stirring, *Biogeosciences*, 11(15), 4077–4098, doi:10.5194/bg-11-
L044 4077-2014, 2014.
L045
L046 Rosso, I., Mazloff, M. R., Verdy, A. and Talley, L. D.: Space and time variability of the Southern Ocean
L047 carbon budget, *J. Geophys. Res. Ocean.*, 122(9), 7407–7432, doi:10.1002/2016JC012646, 2017.
L048
L049 Roy, T., Bopp, L., Gehlen, M., Schneider, B., Cadule, P., Frölicher, T. L., Segschneider, J., Tjiputra, J.,
L050 Heinze, C. and Joos, F.: Regional impacts of climate change and atmospheric CO₂ on future ocean
L051 carbon uptake: A multimodel linear feedback analysis, *J. Clim.*, 24(9), 2300–2318,
L052 doi:10.1175/2010JCLI3787.1, 2011.
L053
L054 Sabine, C. L., Feely, R. A., Gruber, N., Key, R. M., Lee, K., Bullister, J. L., Wanninkhof, R., Wong, C. S.,
L055 Wallace, D. W. R., Tilbrook, B., Millero, F. J., Peng, T. H., Kozyr, A., Ono, T. and Rios, A. F.: The oceanic
L056 sink for anthropogenic CO₂, *Science (80-)*, 305(5682), 367–371, doi:10.1126/science.1097403, 2004.
L057
L058 Sallée, J. B., Wienders, N., Speer, K. and Morrow, R.: Formation of subantarctic mode water in the
L059 southeastern Indian Ocean, *Ocean Dyn.*, 56(5–6), 525–542, doi:10.1007/s10236-005-0054-x, 2006.
L060
L061 Sallée, J. B., Shuckburgh, E., Bruneau, N., Meijers, A. J. S., Bracegirdle, T. J., Wang, Z. and Roy, T.:
L062 Assessment of Southern Ocean water mass circulation and characteristics in CMIP5 models: Historical
L063 bias and forcing response, *J. Geophys. Res. Ocean.*, 118(4), 1830–1844, doi:10.1002/jgrc.20135, 2013.
L064
L065 Sarmiento, J. L. and Gruber, N.: *Ocean Biogeochemical Dynamics*, Carbon N. Y., 67,
L066 doi:10.1063/1.2754608, 2006.
L067
L068 Sarmiento, J. L., Gruber, N., Brzezinski, M. A. and Dunne, J. P.: High-latitude controls of thermocline
L069 nutrients and low latitude biological productivity, *Nature*, 427(6969), 56–60,
L070 doi:10.1038/nature02127, 2004.
L071
L072 Sarmiento, J. L., Hughes, T. M. C., Stouffer, R. J. and Manabe, S.: Simulated response of the ocean carbon
L073 cycle to anthropogenic climate warming, *Nature*, 393(6682), 245–249, doi:10.1038/30455, 1998.
L074
L075 Séférian, R., Bopp, L., Gehlen, M., Orr, J. C., Ethé, C., Cadule, P., Aumont, O., Salas y Méliá, D., Voldoire, A.

L076 and Madec, G.: Skill assessment of three earth system models with common marine biogeochemistry,
L077 *Clim. Dyn.*, 40(9–10), 2549–2573, doi:10.1007/s00382-012-1362-8, 2013.

L078

L079 Segschneider, J. and Bendtsen, J.: Temperature-dependent remineralization in a warming ocean
L080 increases surface pCO₂ through changes in marine ecosystem composition, *Global Biogeochem. Cycles*,
L081 27(4), 1214–1225, doi:10.1002/2013GB004684, 2013.

L082

L083 Son, S. W., Gerber, E. P., Perlwitz, J., Polvani, L. M., Gillett, N. P., Seo, K. H., Eyring, V., Shepherd, T. G.,
L084 Waugh, D., Akiyoshi, H., Austin, J., Baumgaertner, A., Bekki, S., Braesicke, P., Brühl, C., Butchart, N.,
L085 Chipperfield, M. P., Cugnet, D., Dameris, M., Dhomse, S., Frith, S., Garny, H., Garcia, R., Hardiman, S. C.,
L086 Jöckel, P., Lamarque, J. F., Mancini, E., Marchand, M., Michou, M., Nakamura, T., Morgenstern, O., Pitari,
L087 G., Plummer, D. A., Pyle, J., Rozanov, E., Scinocca, J. F., Shibata, K., Smale, D., Teyssdre, H., Tian, W. and
L088 Yamashita, Y.: Impact of stratospheric ozone on Southern Hemisphere circulation change: A
L089 multimodel assessment, *J. Geophys. Res. Atmos.*, 115(19), 1–18, doi:10.1029/2010JD014271, 2010.

L090

L091 Swart, N. C., Fyfe, J. C., Saenko, O. A. and Eby, M.: Wind-driven changes in the ocean carbon sink,
L092 *Biogeosciences*, 11(21), 6107–6117, doi:10.5194/bg-11-6107-2014, 2014.

L093

L094 Tagliabue, A., Mtshali, T., Aumont, O., Bowie, A. R., Klunder, M. B., Roychoudhury, A. N. and Swart, S.: A
L095 global compilation of dissolved iron measurements: Focus on distributions and processes in the
L096 Southern Ocean, *Biogeosciences*, 9(6), 2333–2349, doi:10.5194/bg-9-2333-2012, 2012.

L097

L098 Tagliabue, A., Williams, R. G., Rogan, N., Achterberg, E. P. and Boyd, P. W.: A ventilation-based
L099 framework to explain the regeneration-scavenging balance of iron in the ocean, *Geophys. Res. Lett.*,
L100 41(20), 7227–7236, doi:10.1002/2014GL061066, 2014.

L101

L102 Takahashi, T., Olafsson, J., Goddard, J. G., Chipman, D. W. and Sutherland, S. C.: Seasonal variation of
L103 CO₂ and nutrients in the high-latitude surface oceans: A comparative study, *Global Biogeochem. Cycles*,
L104 7(4), 843–878, doi:10.1029/93GB02263, 1993.

L105

L106 Takahashi, T., Sutherland, S. C., Sweeney, C., Poisson, A., Metzl, N., Tilbrook, B., Bates, N., Wanninkhof,
L107 R., Feely, R. A., Sabine, C., Olafsson, J. and Nojiri, Y.: Global sea-air CO₂ flux based on climatological
L108 surface ocean pCO₂, and seasonal biological and temperature effects, *Deep. Res. Part II Top. Stud.*
L109 *Oceanogr.*, 49, 1601–1622, doi:10.1016/S0967-0645(02)00003-6, 2002.

L110

L111 Takahashi, T., Sutherland, S. C., Wanninkhof, R., Sweeney, C., Feely, R. A., Chipman, D. W., Hales, B.,

l112 Friederich, G., Chavez, F., Sabine, C., Watson, A., Bakker, D. C. E., Schuster, U., Metzl, N., Yoshikawa-
l113 Inoue, H., Ishii, M., Midorikawa, T., Nojiri, Y., Körtzinger, A., Steinhoff, T., Hoppema, M., Olafsson, J.,
l114 Arnarson, T. S., Tilbrook, B., Johannessen, T., Olsen, A., Bellerby, R., Wong, C. S., Delille, B., Bates, N. R.
l115 and de Baar, H. J. W.: Climatological mean and decadal change in surface ocean pCO₂, and net sea-air
l116 CO₂ flux over the global oceans, *Deep. Res. Part II Top. Stud. Oceanogr.*, 56(8–10), 554–577,
l117 doi:10.1016/j.dsr2.2008.12.009, 2009.

l118

l119 Takahashi, T., Sweeney, C., Hales, B., Chipman, D., Newberger, T., Goddard, J., Iannuzzi, R. and
l120 Sutherland, S.: The Changing Carbon Cycle in the Southern Ocean, *Oceanography*, 25(3), 26–37,
l121 doi:10.5670/oceanog.2012.71, 2012.

l122

l123 Taylor, K. E., Stouffer, R. J. and Meehl, G. A.: An overview of CMIP5 and the experiment design, *Bull. Am.*
l124 *Meteorol. Soc.*, 93(4), 485–498, doi:10.1175/BAMS-D-11-00094.1, 2012.

l125

l126 Thomalla, S. J., Fauchereau, N., Swart, S. and Monteiro, P. M. S.: Regional scale characteristics of the
l127 seasonal cycle of chlorophyll in the Southern Ocean, *Biogeosciences*, 8(10), 2849–2866,
l128 doi:10.5194/bg-8-2849-2011, 2011.

l129

l130 Thompson, D. W. J., Solomon, S., Kushner, P. J., England, M. H., Grise, K. M. and Karoly, D. J.: Signatures
l131 of the Antarctic ozone hole in Southern Hemisphere surface climate change, *Nat. Geosci.*, 4(11), 741–
l132 749, doi:10.1038/ngeo1296, 2011.

l133

l134 Vichi, M., Pinardi, N. and Masina, S.: A generalized model of pelagic biogeochemistry for the global
l135 ocean ecosystem. Part I: Theory, *J. Mar. Syst.*, 64(1–4), 89–109, doi:DOI
l136 10.1016/j.jmarsys.2006.03.006, 2007.

l137

l138 Visinelli, L., Masina, S., Vichi, M., Storto, A. and Lovato, T.: Impacts of data assimilation on the global
l139 ocean carbonate system, *J. Mar. Syst.*, 158, 106–119, doi:10.1016/j.jmarsys.2016.02.011, 2016.

l140

l141 Wanninkhof, R., Asher, W. E., Ho, D. T., Sweeney, C. and McGillis, W. R.: Advances in Quantifying Air-Sea
l142 Gas Exchange and Environmental Forcing, *Ann. Rev. Mar. Sci.*, 1(1), 213–244,
l143 doi:10.1146/annurev.marine.010908.163742, 2009.

l144

l145 Wanninkhof, R., Park, G. H., Takahashi, T., Sweeney, C., Feely, R., Nojiri, Y., Gruber, N., Doney, S. C.,
l146 McKinley, G. A., Lenton, A., Le Quere, C., Heinze, C., Schwinger, J., Graven, H. and Khatiwala, S.: Global
l147 ocean carbon uptake: Magnitude, variability and trends, *Biogeosciences*, 10(3), 1983–2000,

L148 doi:10.5194/bg-10-1983-2013, 2013.

L149

L150 Williams, N. L., Juranek, L. W., Feely, R. A., Johnson, K. S., Sarmiento, J. L., Talley, L. D., Dickson, A. G.,
L151 Gray, A. R., Wanninkhof, R., Russell, J. L., Riser, S. C. and Takeshita, Y.: Calculating surface ocean pCO₂
L152 from biogeochemical Argo floats equipped with pH: An uncertainty analysis, *Global Biogeochem.*
L153 *Cycles*, 31(3), 591–604, doi:10.1002/2016GB005541, 2017.

L154

L155 Young, I. R.: Seasonal Variability of the Global Ocean Wind and Wave Climate, *Int. J. Clim.*, 19(July
L156 2015), 931–950, doi:10.1002/(SICI)1097-0088(199907)19, 1999.

L157

L158 Zahariev, K., Christian, J. R. and Denman, K. L.: Preindustrial, historical, and fertilization simulations
L159 using a global ocean carbon model with new parameterizations of iron limitation, calcification, and
L160 N₂fixation, *Prog. Oceanogr.*, 77(1), 56–82, doi:10.1016/j.pocean.2008.01.007, 2008.

L161

L162 Zickfeld, K., Fyfe, J. C., Eby, M. and Weaver, A. J.: Comment on “Saturation of the southern ocean CO₂
L163 sink due to recent climate change”;;, *Science*, 319(5863), 570; author reply 570,
L164 doi:10.1126/science.1146886, 2008.

L165

L166

L167

L168

L169

L170

L171

L172

L173

L174

L175

L176

L177

L178

L179

L180

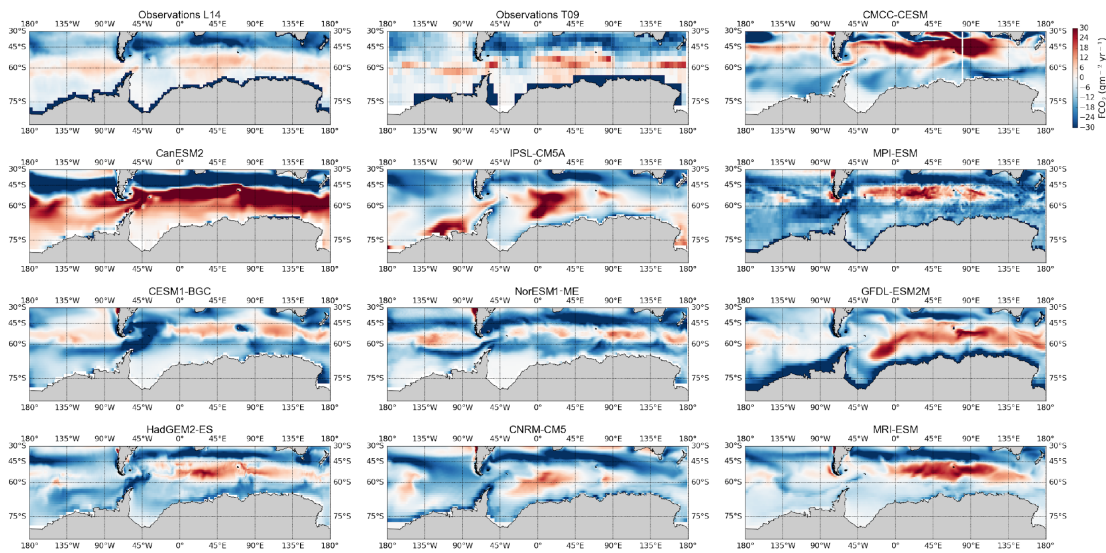
L181

L182

L183

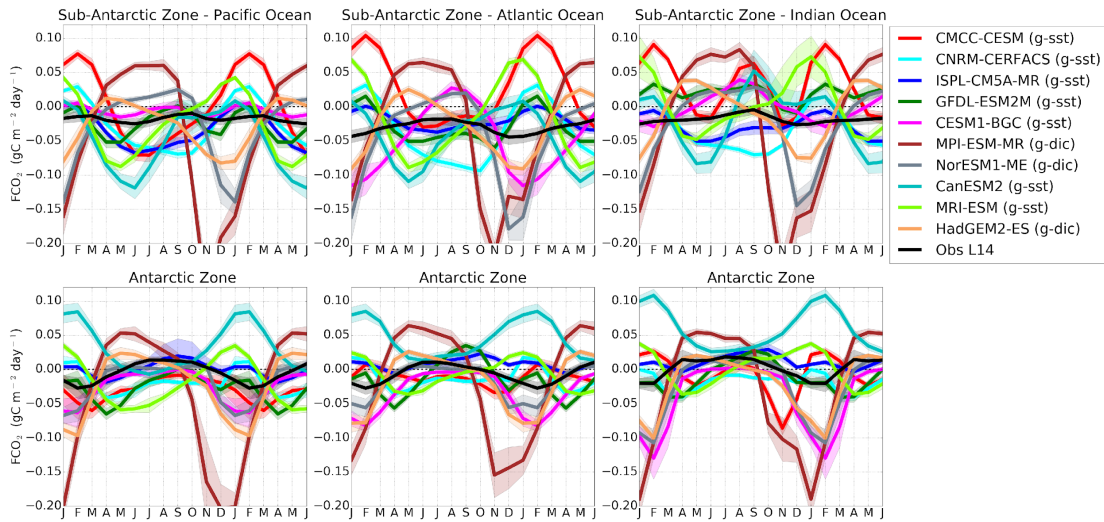
L184
L185
L186
L187
L188
L189

Figures



L190
L191
L192
L193
L194
L195
L196
L197
L198
L199
L200
L201
L202
L203
L204
L205
L206

Fig. 1: The annual mean climatological distribution Sea-Air CO₂ Flux (FCO₂, in gC m⁻² yr⁻¹) for observations (L14: Landschützer et al., 2014 and T09: Takahashi et al., 2009) and 10 CMIP5 models over 1995 – 2005. CMIP5 models broadly capture the spatial distribution of FCO₂ with respect to L14 and T09, however, they also show significant differences in space and magnitude between the basins of the Southern Ocean with a few exceptions.



[207

[208

[209

Fig. 2: Seasonal cycle of Sea-Air CO₂ Flux (FCO₂, in gC m⁻² yr⁻¹) in observations and 10 CMIP5 models in the Sub-Antarctic and Antarctic zones of the Pacific Ocean (first column), Atlantic Ocean (second column) and Indian Ocean (third column). The shaded area shows the temporal standard deviation over the considered period (1995 – 2005), g-sst and g-dic shows the clustering of CMIP5 models into group-SST and group-DIC as shown in Fig. 3 (section 3.2).

[214

[215

[216

[217

[218

[219

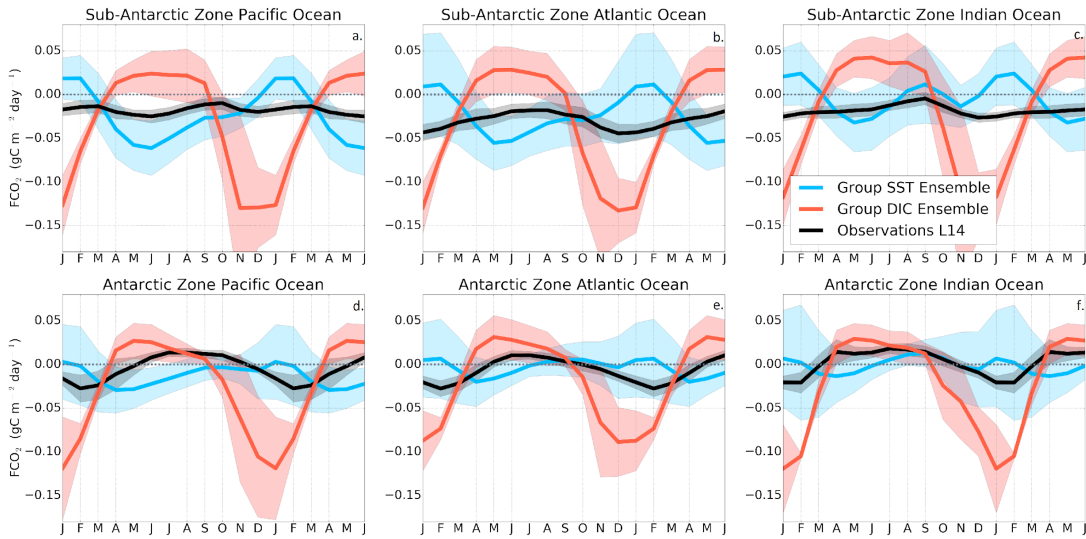
[220

[221

[222

[223

[224



L225

L226

Fig. 3. Seasonal cycle of the equally-weighted ensemble means of FCO_2 ($\text{gC m}^{-2} \text{yr}^{-1}$) from Fig. 2 for group

L227

DIC models (MPI-ESM, HadGEM-ES and NorESM) and group SST models (GFDL-ESM2M, CMCC-CESM,

L228

CNRM-CERFACS, IPSL-CM5A-MR, CESM1-BGC, NorESM2, MRI-ESM and CanESM2). The shaded areas show

L229

the ensemble standard deviation. The black line is the Landschützer et al. (2014) observations.

L230

L231

L232

L233

L234

L235

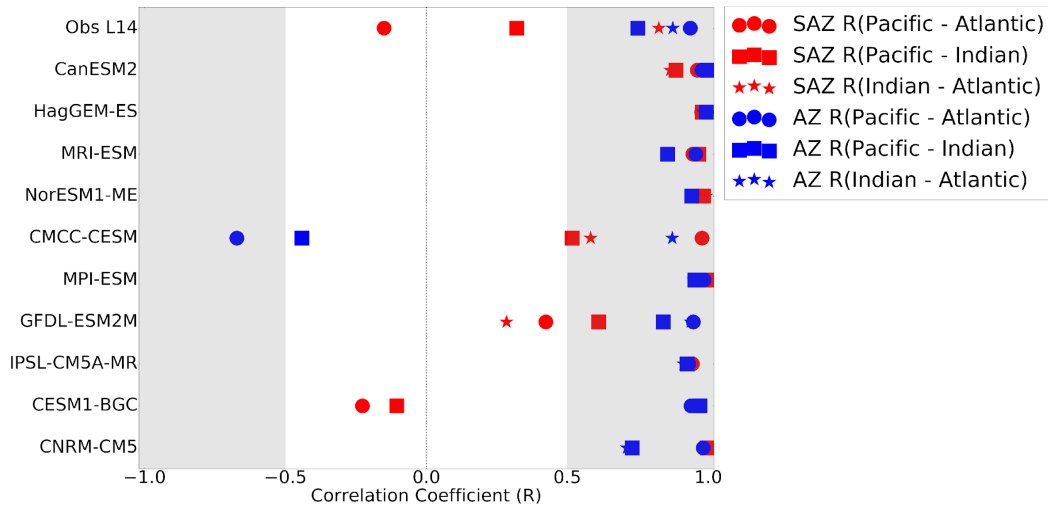
L236

L237

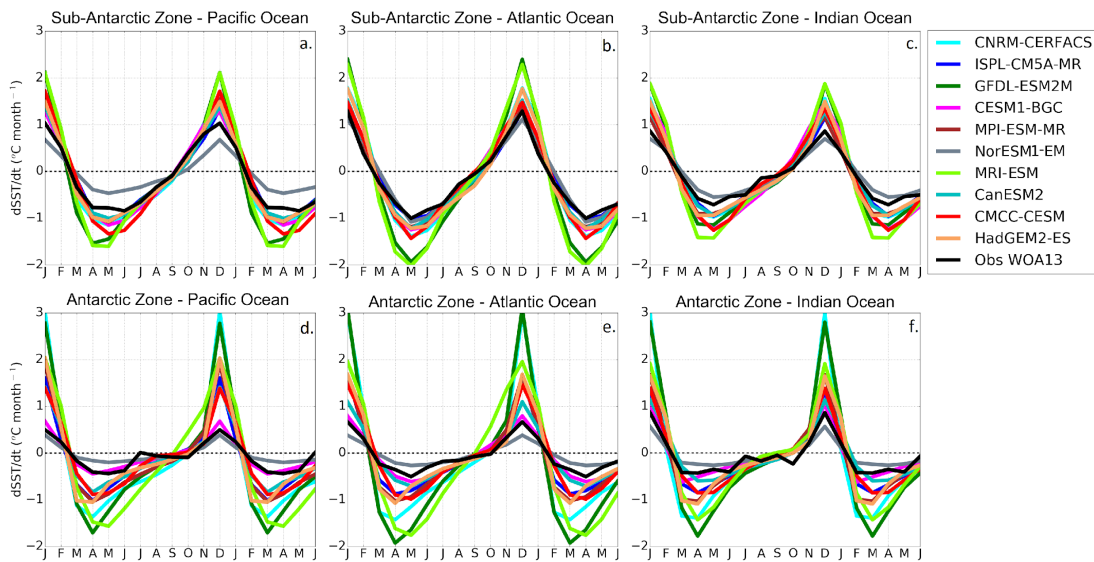
L238

L239

L240

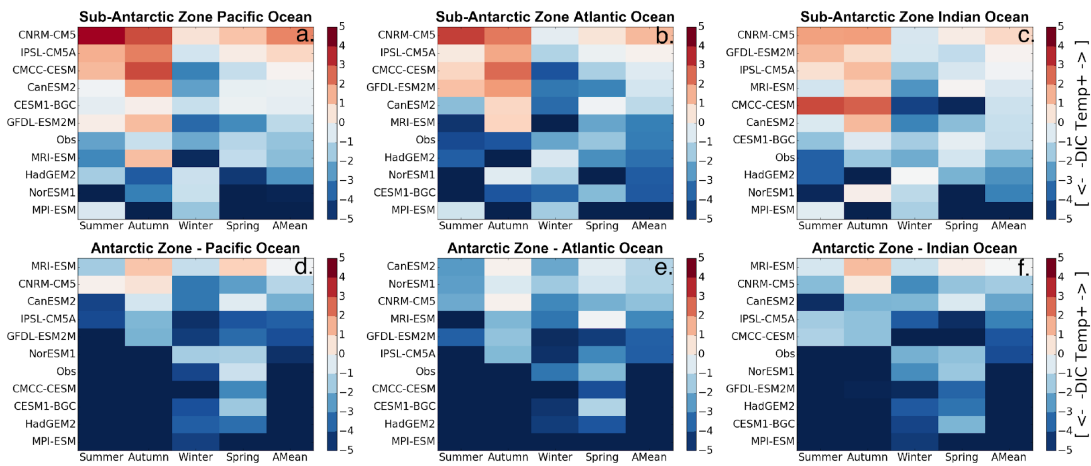


[241]
 [242] **Fig. 4:** The correlation coefficients (R) of basin – basin seasonal cycles of FCO₂ for observations
 [243] (Landschützer et al., 2014) and 10 CMIP5 models in the three basins of the Southern Ocean i.e. Pacific,
 [244] Atlantic and Indian basin.
 [245]
 [246]
 [247]
 [248]
 [249]
 [250]
 [251]
 [252]
 [253]
 [254]
 [255]
 [256]
 [257]
 [258]
 [259]
 [260]
 [261]
 [262]
 [263]
 [264]



[265]
 [266] **Fig. 5:** Mean seasonal cycle of the estimated rate of change of sea-surface temperature ($dSST/dt$, $^{\circ}C$
 [267] $month^{-1}$) for the Sub-Antarctic and Antarctic zones of the Pacific Ocean (first column), Atlantic Ocean
 [268] (second column) and Indian Ocean (third column).

[269]
 [270]
 [271]
 [272]
 [273]
 [274]
 [275]
 [276]
 [277]
 [278]
 [279]
 [280]
 [281]
 [282]
 [283]



[284

[285

[286

[287

[288

[289

[290

[291

[292

[293

[294

[295

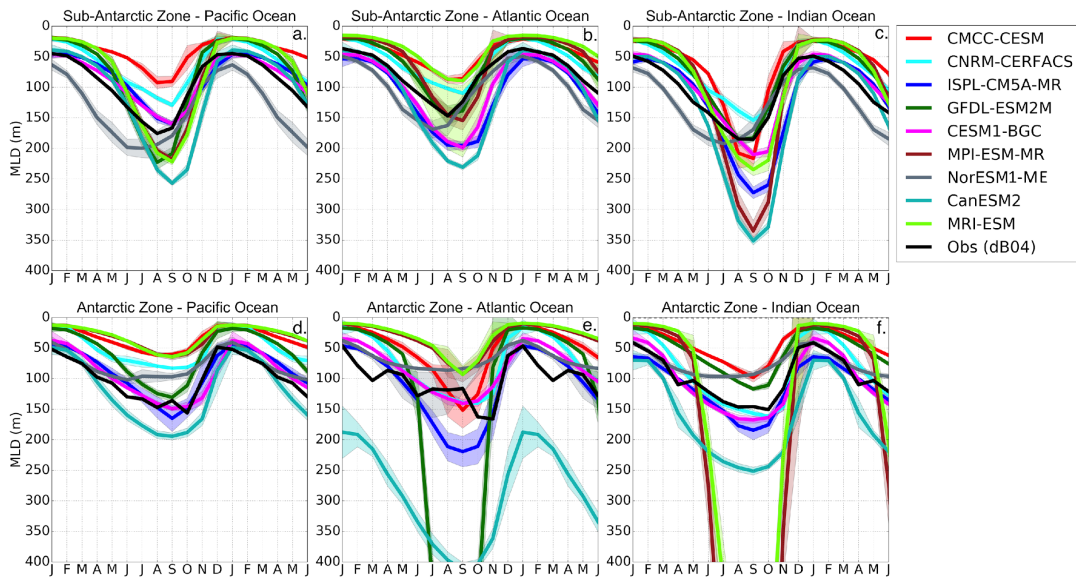
[296

[297

[298

[299

Fig. 6: Mean seasonal and annual values of the DIC–temperature control index (M_{T-DIC}). The increase in the red color intensity indicates increase in the strength of the temperature driver and the blue intensity shows the strength of the DIC driver. The models are sorted according to the annual mean value of the indicator presented in the last column (Amean).



[300

[301

[302 **Fig. 7:** Seasonal cycle of the Mixed Layer Depth (MLD) in the Sub-Antarctic and Antarctic zones of the Pacific
 [303 Ocean (first column), Atlantic Ocean (second column) and Indian Ocean (third column).

[304

[305

[306

[307

[308

[309

[310

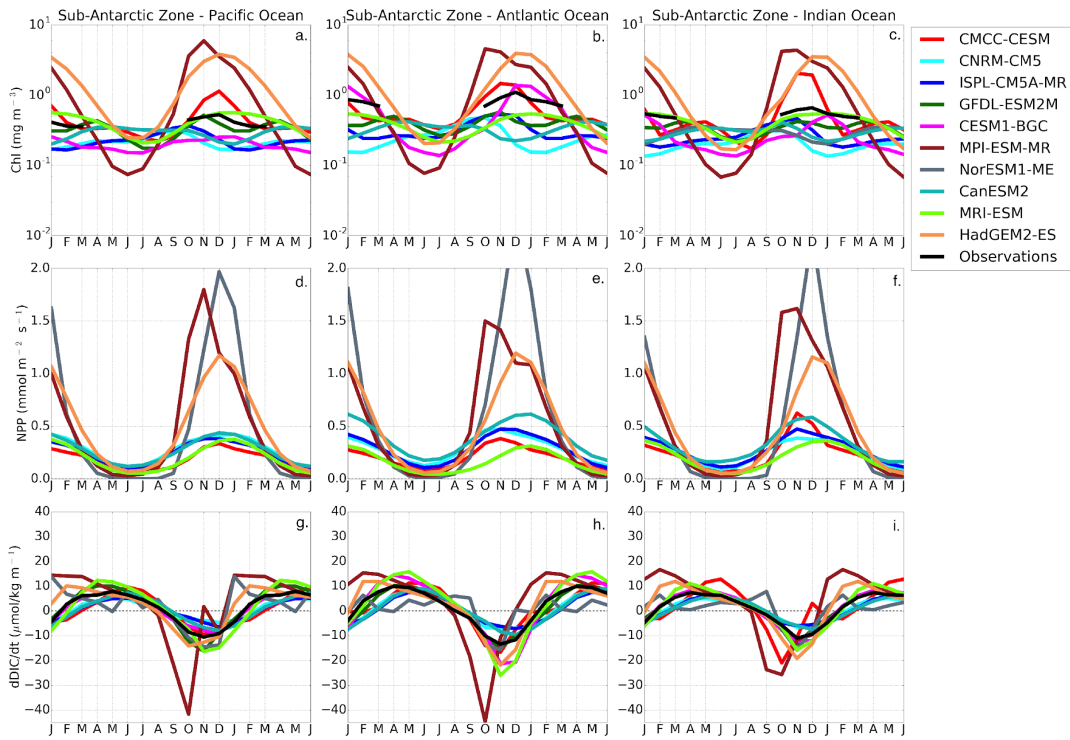
[311

[312

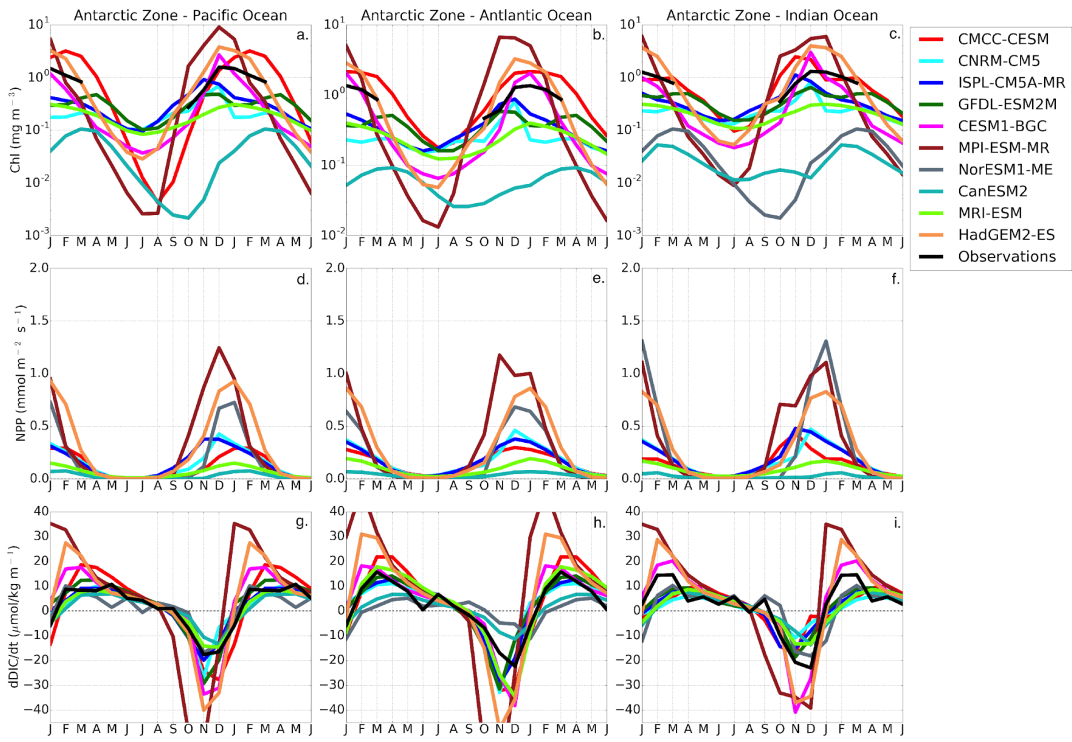
[313

[314

[315



[316]
 [317] **Fig. 8:** The seasonal cycle of chlorophyll (mg m^{-3}), Net Primary Production ($\text{mmol m}^{-2} \text{s}^{-1}$) and the surface
 [318] rate of change of DIC ($\mu\text{mol kg}^{-1} \text{month}^{-1}$) in the Sub-Antarctic zone of the Pacific Ocean (first column),
 [319] Atlantic Ocean (second column) and Indian Ocean (third column).
 [320]
 [321]
 [322]
 [323]
 [324]
 [325]



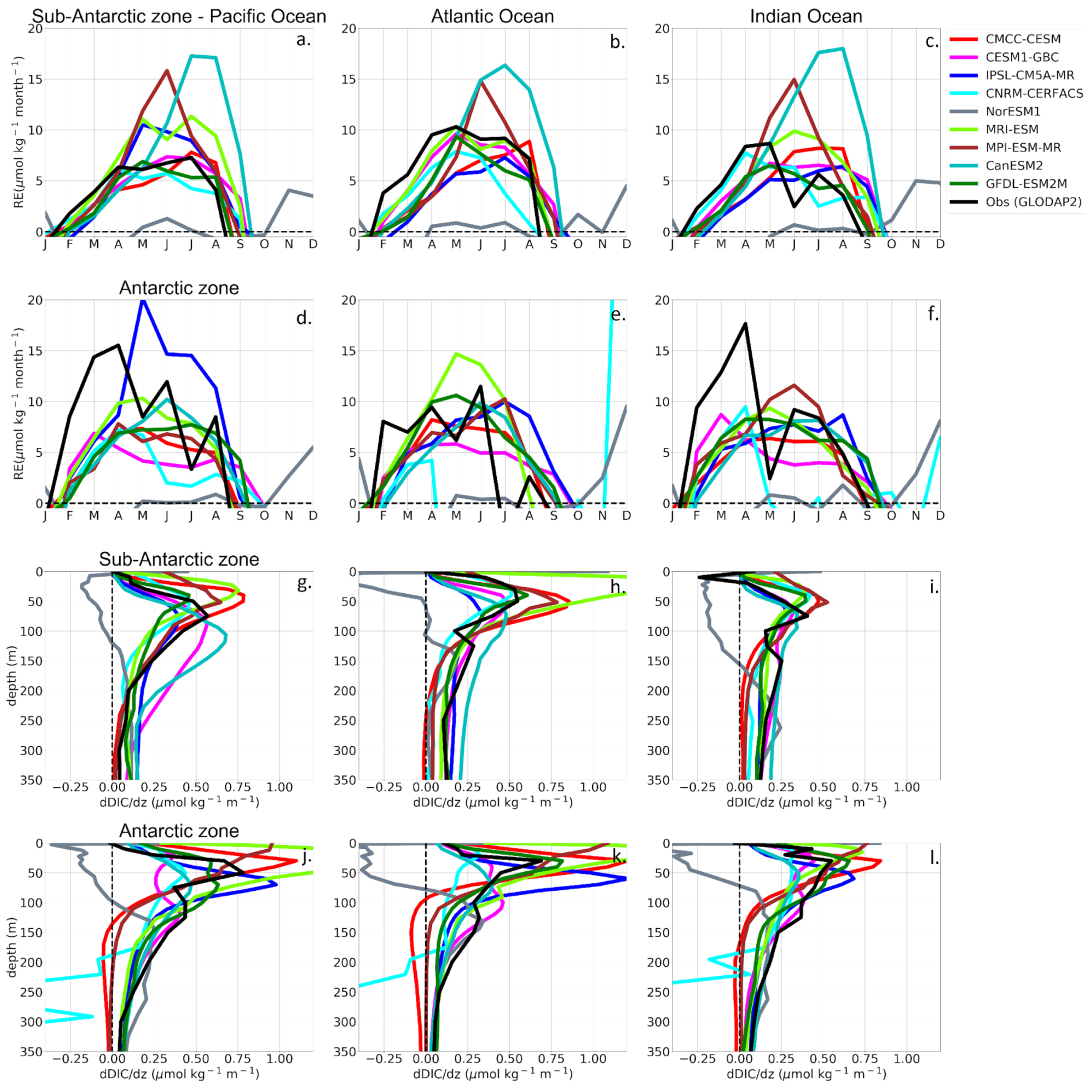
[326

[327

Fig. 9 Same as Fig. 8 for the Antarctic zone.

[328

[329



L330
 L331 **Fig. 10:** (a-f) Estimated DIC entrainment fluxes (mol kg month^{-1}) at the base of the mixed layer and (g-i)
 L332 vertical DIC gradients ($\mu\text{mol kg}^{-1} \text{m}^{-1}$) in the Sub-Antarctic and Antarctic zone of the Pacific Ocean (first
 L333 column), Atlantic Ocean (second column) and Indian Ocean (third column).

L334
 L335
 L336
 L337
 L338
 L339
 L340
 L341

L342 **Table 2:** Sea-Air CO₂ fluxes (Pg C yr⁻¹) annual mean uptake in the Southern Ocean (first column), here
 L343 defined as south of the Sub-tropical front, Sub-Antarctic zone (second column) and Antarctic zone (third
 L344 column). The third and fourth column shows the Pattern Correlation Coefficient (PCC) and Root Mean
 L345 Square Error (RMSE) for the whole Southern Ocean for each model. Observations here refer to
 L346 Landschützer et al., 2014.

| Model | Southern Ocean | Sub-Antarctic zone | Antarctic zone | PCC | RMSE |
|--------------|----------------|--------------------|----------------|-------|------|
| CNRM-CM5 | -0.823 ± 0.003 | -0.682 ± 0.002 | -0.122 ± 0.001 | 0.44 | 17.9 |
| GFDL-ESM2M | -0.161 ± 0.005 | -0.074 ± 0.004 | -0.077 ± 0.002 | 0.43 | 8.47 |
| HadGEM2-ES | -0.489 ± 0.005 | -0.284 ± 0.003 | -0.197 ± 0.001 | 0.55 | 10.9 |
| IPSL-CM5A-MR | -0.496 ± 0.003 | -0.582 ± 0.006 | 0.101 ± 0.003 | 0.53 | 10.5 |
| MPI-ESM-MR | -0.870 ± 0.006 | -0.530 ± 0.002 | -0.326 ± 0.002 | 0.37 | 9.87 |
| MRI-ESM | -0.048 ± 0.002 | 0.022 ± 0.003 | -0.070 ± 0.001 | 0.36 | 15.6 |
| NorESM1 | -0.699 ± 0.004 | -0.412 ± 0.003 | -0.270 ± 0.002 | 0.60 | 8.96 |
| CESM1-BGC | -0.532 ± 0.006 | -0.132 ± 0.003 | -0.385 ± 0.004 | 0.47 | 9.15 |
| CMCC-CESM | 0.121 ± 0.006 | 0.367 ± 0.004 | -0.225 ± 0.003 | -0.09 | 17.9 |
| CanESM2 | -0.058 ± 0.008 | -0.720 ± 0.006 | 0.661 ± 0.004 | 0.54 | 19.5 |
| Observations | -0.253 ± 0.3 | -0.296 ± 0.3 | 0.053 ± 0.3 | | |

L347